MONITORING FATIGUE CRACKS IN RIVETED AEROSPACE PLATES USING NONLINEAR ULTRASONIC TECHNIQUES

by

Bo Hu

A Thesis Submitted to the Faculty of the

DEPARTMENT OF AEROSPACE & MECHANICAL ENGINEERING

In Partial Fulfillment of the Requirements

For the Degree of

MASTER OF SCIENCE

In the Graduate College

THE UNIVERSITY OF ARIZONA

2024

THE UNIVERSITY OF ARIZONA
GRADUATE COLLEGE

As members of the Master's Committee, we certify that we have read the thesis prepared by *Bo Hu*, titled *Monitoring Fatigue Cracks in Riveted Plates Using Nonlinear Ultrasonic Techniques* and recommend that it be accepted as fulfilling the dissertation requirement for the Master's Degree.

Tribikram Kundu (Apr 9, 2024 10:57 PDT) Date: Apr 9, 2024
Prof. Tribikram Kundu

Date: Apr 9, 2024
Prof. Erdogan Madenci

Olesya Zhupanska (Apr 11, 2024 20:47 PDT) Date: Apr 11, 2024
Prof. Olesya Zhupanska

Final approval and acceptance of this thesis is contingent upon the candidate's submission of the final copies of the thesis to the Graduate College.

I hereby certify that I have read this thesis prepared under my direction and recommend that it be accepted as fulfilling the Master's requirement.

Tribikram Kundu (Apr 9, 2024 10:57 PDT) Date: Apr 9, 2024
Prof. Tribikram Kundu
Master's Thesis Committee Chair
Department of Civil & Architectural Engineering & Mechanics
Department of Aerospace & Mechanical Engineering
Department of Materials Science & Engineering

ACKNOWLEDGMENTS

My sincere and hearty thanks and appreciations go firstly to my academic supervisor, Dr. Tribikram Kundu, for his kindness, illuminating guidance and profound knowledge. His insightful suggestions and encouragement have provided me with invaluable insights into the theoretical basis, experimentation, and analysis. Working on a very busy schedule, he dedicated time to carefully read my thesis and offer detailed feedback. Without his keen insights and constant encouragement, this thesis would not have been completed. Studying under his guidance and supervision has been a tremendous privilege and source of joy. Moreover, I am deeply honored to have benefited from his character and diligence, qualities that I will cherish for a lifetime. Dr. Tribikram Kundu not only introduced me to this exciting world of research but also profoundly impacted my life's trajectory. My gratitude to him is boundless.

I also want to express my appreciation to Dr. Erdogan Madenci and Dr. Olesya Zhupanska for their dedicated service in my committee, and providing me with their invaluable time and insightful advice for refining this research. Additionally, I would like to thank the aforementioned two professors, as well as Dr. Samy Missoum, for their outstanding courses. These courses have significantly enriched my knowledge and understanding in the field of mechanical engineering.

Sincere thanks to Dr. Hee-Jeong Kim for offering me the research assistant position and providing financial support, which made this graduate study possible for me.

Many thanks to Dr. Abhijit Mahalanobis and Dr. Andrew Wessman for allowing me to enroll in their courses during my first semester, despite being more than two weeks late. Their excellent courses have deepened my understanding in machine learning and metal corrosion.

Special thanks to Dr. Umar Amjad and Dr. SeHyuk Park for their assistance and inspiration in the testing and experimental design. And, thank Dr. Jeong-Beom Ihn of the Boeing Corporation for providing the specimen used in this research.

Immense thanks to Mr. Jon Heine, for the help and support he have provided me in all aspects of my life during my studies and living in Tucson. I would also like to thank all my brothers and sisters in ISF.

My sincere gratitude to my mother, Decui Liu, and father, Yougu Hu, who guided and supported me throughout my life, as well as my mother-in-law Lianhua Wang, and father-in-law Zilin Yang. Also, to my wife Yuanrong Yang and sister Xiaoling Hu, for their unwavering support and encouragement. Thank you, my family, for believing in me and your unconditional love. You are the driving force behind my perseverance in completing my study and this thesis.

DEDICATION

To

My father Youguo Hu and mother Decui Liu

TABLE OF CONTENTS

ABSTRACT

Aluminum structures are commonly used in aircraft due to their lightweight and corrosion resistance compared to other metals. Often multi-layered aluminum plates are joined by rivets which are prone to fatigue crack formation in aircrafts. Therefore, the detection and monitoring of fatigue cracks at rivet joints in aluminum structures are crucial for ensuring flight safety. In this study, piezoelectric sensors are used to generate and detect Lamb waves on aluminum plates with rivet joints. The feasibility of a newly developed nonlinear ultrasonic technique called Sideband Peak Count (SPC) technique is investigated for detecting fatigue cracks near these joints. To overcome some limitations of existing SPC-I and SPI ((a modified version of SPC-I) techniques in capturing harmonic and modulating wave frequencies due to material nonlinearity, another index called the Sideband Intensity Index (SII) is introduced. Comparative analysis of SII with existing SPC-I and SPI techniques show some advantages of the SII technique. Research findings demonstrate that the SII technique can reliably detect fatigue cracks around rivet joints on aluminum plates. This study offers a more efficient method for detecting critical fatigue cracks in rivet joints.

1. INTRODUCTION

Aluminum is most popular metal for aircraft construction due to its combination of lightweight and corrosion resistance properties. However, aluminum has a relatively low melting point compared to other metals. Welding involves high temperatures, which can cause distortion, warping, and even weakening of aluminum in the heat-affected zone. Riveting doesn't require such high level of heat and thus can avoid the heat related issues. Hence, riveting is often preferred over welding in the aerospace industries when dealing with aluminum.

Figure 1.1. Fatigue cracked fuselage on the Southwest Boeing 737.

However, aircraft structures experience alternating or cyclic loads in flight, which can accumulate stress induced damage at riveted joints. This can evolve into fatigue cracks, which gradually expand and may lead to component failure and threaten to flight safety. Figure 1.1 shows a

Southwest Airlines plane (Boeing 737) landed at Yuma International Airport in Arizona in 2011 following an incident where a fatigue-induced crack caused a tear in its fuselage during flight [1]. Within the aviation domain, historical records have consistently reported occurrences of aircraft skin failures attributed to fatigue cracks at rivet connections. On August 22, 1981, a Boeing 737–200, operating as Far Eastern Air Transport Flight 103 within Taiwan, experienced a catastrophic fuselage failure due to fatigue. This failure occurred in a lap joint underneath the first-class cabin, likely a result of undetected cracks caused by numerous pressurization flight cycles. The lower fuselage section tore away, causing the cockpit to bend downward and the compression failure of floor beams, ultimately leading to the midair breakup of the aircraft [2].

Figure 1.2. Aircraft fuselage failure on the Aloha Airlines flight 243.

On April 28, 1988, passengers on an Aloha Airlines Boeing 737 faced a life-threatening situation when the aircraft's roof tore off at 24,000 feet, refer to Figure 1.2. Enduring hurricane-force winds and freezing temperatures, passengers and crew lived on the edge for thirteen terrifying minutes, with only the buckling floor beams providing any assurance of survival [3].

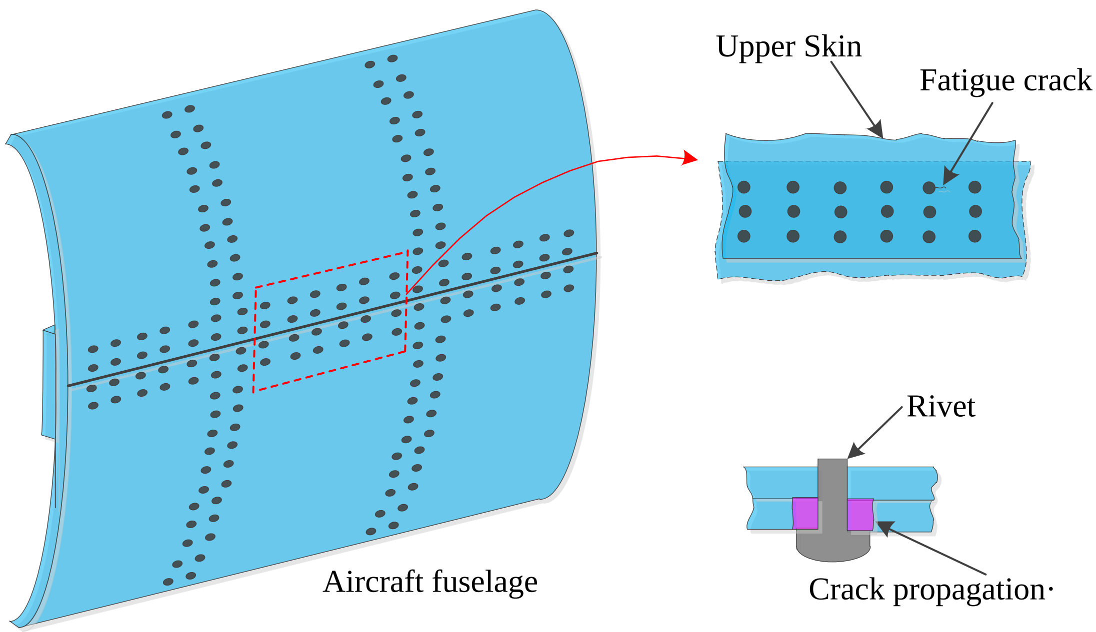

Figure 1.3. Typical lap joint and rivet on aircraft fuselage.

Figure 1.3. illustrates typical overlap connections and rivets used in the aircraft fuselages of Southwest Boeing 737. The fatigue vulnerability in this type of fuselage resides in the lap joint between the upper and lower aluminum skins. This region can potentially initiate fatigue cracks under stress, which may subsequently propagate along the row of rivets in both directions. It is not confined to the Boeing 737 aircraft model only; fatigue cracks at rivet connections in the fuselage skin have been observed in various other aircraft models also, with numerous instances of accidents resulting from these issues.

Therefore, the development of structural health monitoring (SHM) techniques for fatigue cracks in riveted joints is essential for flight safety. However, much of the research literature has been focused on crack detection in plate and sheet structures using Lamb waves to achieve the basic goals of non-destructive evaluation (NDE) or SHM. Chang and Mal (1999) theoretically and experimentally investigated Lamb waves propagating in plates with circular holes. The time histories and amplitude spectra of the transmitted and reflected waves are compared with those calculated from the hybrid model [4]. Ihn and Chang (2008) developed a piezoelectric-based technique for monitoring fatigue crack growth in metal structures, using embedded actuators to generate diagnostic signals. The method includes signal processing and a physics-based damage index, demonstrating strong correlation between built-in piezoceramics measurements and actual crack growth. Parametric studies further validate the technique's sensitivity [5-7]. He et al. (2013) employed embedded PZT sensors for in-situ NDE during fatigue loading of lap joints. They utilized multi-feature method using multivariate regression for predicting crack lengths, validated with various lap joint conditions. It is found that the fatigue crack lengths are correlated with three main features of the signal, i.e., correlation coefficient, amplitude change, and the phase change [8]. In these studies, damage assessment was mainly based on utilizing linear ultrasound parameters, such as direction and strength of scattered waves, change in velocity & attenuation of ultrasonic waves.

However, linear ultrasonic techniques can only capture changes in linear parameters, and defects much smaller than the signal wavelength, usually have little effect on these linear parameters. Therefore, monitoring fatigue cracks at their initial stages using linear ultrasonic techniques has been challenging. Recent studies have highlighted that nonlinear ultrasonic techniques, such as the

Higher Harmonic Generation (HHG) technique, Frequency Modulation (FM) technique and Nonlinear Impact Resonance Acoustic Spectroscopy (NIRAS), are much more sensitive and useful for monitoring micro-cracks when compared with the conventional linear methods.

The HHG technique has been applied for evaluating acoustic nonlinearity in a variety of materials [9-16]. The second and third harmonics have demonstrated sensitivity to fatigue-induced damage in various materials. The limitations of this technique stem from its difficulty in handling relatively complex structures and often struggling to ensure the reliability and repeatability of measurement results [17-22]. The FM technique uses two frequencies: a high-amplitude, low-frequency pumping wave and a low-amplitude, high-frequency probing wave. This frequency setup offers advantages by avoiding uniform paths, mitigating reflecting boundary concerns, and sidestepping high voltages and nonlinear signals that could affect sensitivity. This technique is more versatile and works effectively for characterizing bulk materials, but it encounters challenges when applied to monitoring plates, rods, and pipes [23-28]. The NIRAS simultaneously monitors resonant frequency shifts and attenuation changes as the excitation amplitude increases. The resonance frequencies of specimens change with the intensity of impacts only for nonlinear specimens. This technique is effective for monitoring distributed micro-cracks but less efficient for tracking the progression of macro-cracks [29-30].

Despite several advancements reported in these nonlinear ultrasonic techniques, challenges still exist for their practical field application. The recently developed nonlinear ultrasonic technique, Sideband Peak Count (SPC), along with its derivatives including the Sideband Peak Count-Index (SPC-I) and Sideband Peak Intensity (SPI), demonstrated enhanced robustness and inherent advantages compared to other linear and nonlinear methods. Embraced by numerous research teams, SPC-based techniques have been used to identify and track defects in a diverse set of materials, including cement mortar, concrete, metals, and polymer composites [31-49]. These investigations indicated that the Sideband Peak Count-based techniques are capable of reliably and consistently detecting the initiation and progression of damage in various types of materials. However, monitoring fatigue cracks in a rivet-jointed structures presents significantly greater challenges. Hence, there is considerable interest in investigating whether the newly developed SPC-based technique is applicable for monitoring the riveted structures.

In this research, PZT (lead zirconium titanate) transducers are used for both Lamb wave generation and detection in an aluminum plate with rivet joints. Considering the challenges in monitoring fatigue cracks initiated around rivet joints, the SPC based nonlinear ultrasonic techniques are adopted. Additionally, a more general index, Sideband Intensity Index (SII) is developed and compared with the results obtained from SPC-I and SPI techniques. Some inherent limitations of SPC-I and SPI techniques in fully accounting for harmonic frequencies and modulating wave frequencies induced by material nonlinearity are overcome in the Sideband Intensity Index (SII) measurement. The effectiveness of the SII technique is verified by comparing the results generated by these three algorithms. The findings from this study demonstrate the potential of the SII to enhance the detection of fatigue cracks around rivet joints on aluminum plates.

2. THEORETICAL BASIS

When a wave of a single frequency propagates through a nonlinear material, it generates waves with new frequencies. This phenomenon is commonly known as higher harmonic generation (HHG). Additionally, if a nonlinear material is excited by harmonic waves containing two or more frequencies, it results in both higher harmonic generation (HHG) and the generation of modulated wave frequencies, with the peaks of these modulated wave frequencies are known as sideband peaks and this process is called sideband peak generation (SPG). The existence of HHG and SPG can indeed be derived mathematically, as demonstrated bellow. First, the examination will focus on single-frequency and two-frequency scenarios. The detail derivations for these two scenarios were presented by Kundu et al. [33-34]. Then, the concept will be extended to encompass a set of frequencies in a more general case.

2.1. Proof of Higher Harmonic Generation (HHG) for Single Frequency Case

The mathematical proof of higher harmonic generation can be derived with a nonlinear material excited by a wave of a single frequency. When a nonlinear material is excited by a harmonic wave with a single frequency of f, displacement field u in the material can be expressed as,

$$u(x,t) = A(x)\,sin(\omega t) + B(x)\,cos(\omega t) \tag{1}$$

where $\omega = 2\pi f$ is the angular frequency, and the one-dimensional strain field ε for the input displacement field of Eq. (1) is given as,

$$\varepsilon(x,t) = \frac{\partial u(x,t)}{\partial x} = A'(x)\,sin(\omega t) + B'(x)\,cos(\omega t) \tag{2}$$

Following the traditional nonlinear quadratic stress-strain relation, the harmonic stress field is given as the follows:

$$\sigma(x,t) = E_0\varepsilon(x,t) - E_1\,\varepsilon^2(x,t)$$
$$= E_0\{A'(x)\,sin(\omega t) + B'(x)\,cos(\omega t)\}$$
$$-E_1\left[\frac{\{A'(x)\}^2\{1-cos(2\omega t)\}}{2} + \frac{\{B'(x)\}^2\{1-cos(2\omega t)\}}{2} + A'(x)B'(x)sin(2\omega t)\right] \quad (3)$$

Eq. (3) clearly shows that if a nonlinear material is excited by a harmonic wave of single frequency ω then the wave of frequency 2ω (second higher harmonic) is generated (Figure 2.1). Moreover, if the stiffness modulus is to be a higher-order function of strain, then the stress-strain relation will contain higher-order terms. In other words, when a nonlinear material is excited by a wave of single frequency, which higher harmonics are produced, depends on the order of nonlinearity of the material.

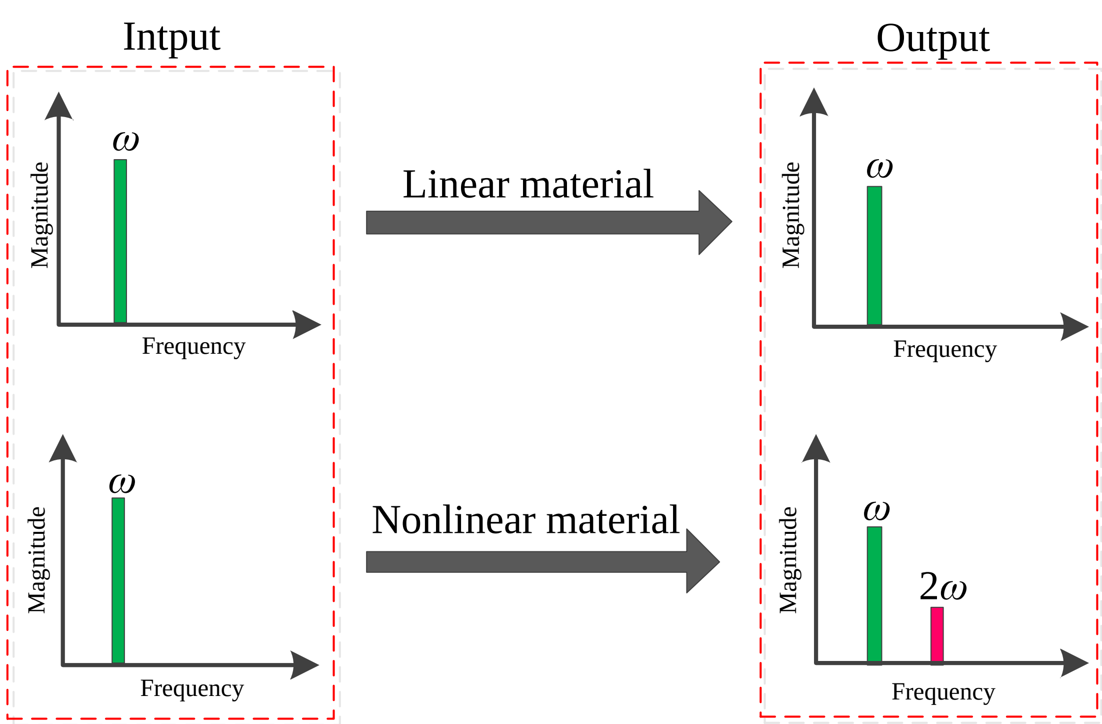

Figure 2.1 Illustration of higher harmonic generation

2.2. Proof of Sideband Peak Generation (SPG) for Two-Frequency Case

Similarly, the mathematical proof of sideband generation can be derived with a nonlinear material excited by waves of two different frequencies. The cosine terms in this derivation are omitted for the simplicity of the expressions. When a nonlinear material is excited by harmonic waves with two different frequencies of f_1 and f_2, the displacement fields u_1 and u_2 in the material can be expressed as,

$$u_1(x,t) = A_1(x)\, sin(\omega_1 t) \tag{4}$$

$$u_2(x,t) = A_2(x)\, sin(\omega_2 t) \tag{5}$$

where $\omega_1 = 2\pi f_1$ and $\omega_2 = 2\pi f_2$ are the angular frequencies. Then the total displacement field is,

$$u(x,t) = u_1(x,t) + u_2(x,t) = A_1(x)\, sin(\omega_1 t) + A_2(x)\, sin(\omega_2 t) \tag{6}$$

The one-dimensional strain field ε for the input displacement field of Eq. (6) is given as,

$$\varepsilon(x,t) = \frac{\partial u(x,t)}{\partial x} = A_1'(x)\, sin(\omega_1 t) + A_2'(x)\, sin(\omega_2 t) \tag{7}$$

Following the classical nonlinear quadratic stress-strain relation, the harmonic stress field is given as,

$$\begin{aligned}\sigma(x,t) &= E_0 \varepsilon(x,t) - E_1\, \varepsilon^2(x,t) \\ &= E_0\{A_1'(x)\, sin(\omega_1 t) + A_2'(x)\, sin(\omega_2 t)\} \\ &\quad - E_1 \begin{bmatrix} \frac{\{A_1'(x)\}^2\{1-cos(2\omega_1 t)\}}{2} + \frac{\{A_2'(x)\}^2\{1-cos(2\omega_2 t)\}}{2} \\ +A_1'(x)A_2'(x)\{\cos(\omega_1-\omega_2)t - \cos(\omega_1+\omega_2)t\} \end{bmatrix}\end{aligned} \tag{8}$$

Eq. (8) clearly shows that if a nonlinear material is excited by harmonic waves of two different frequencies ω_1 and ω_2 then the waves of frequencies $2\omega_1$ and $2\omega_2$ (second higher harmonics) as well as $\omega_1 \pm \omega_2$ (modulated wave frequencies) are generated (Figure 2.2). The modulated wave frequency peaks are called sideband peaks or simply sidebands. The detail derivations (Eqs. 1 to 8) of sections 2.1 and 2.2 were presented by Kundu et al. [33-34].

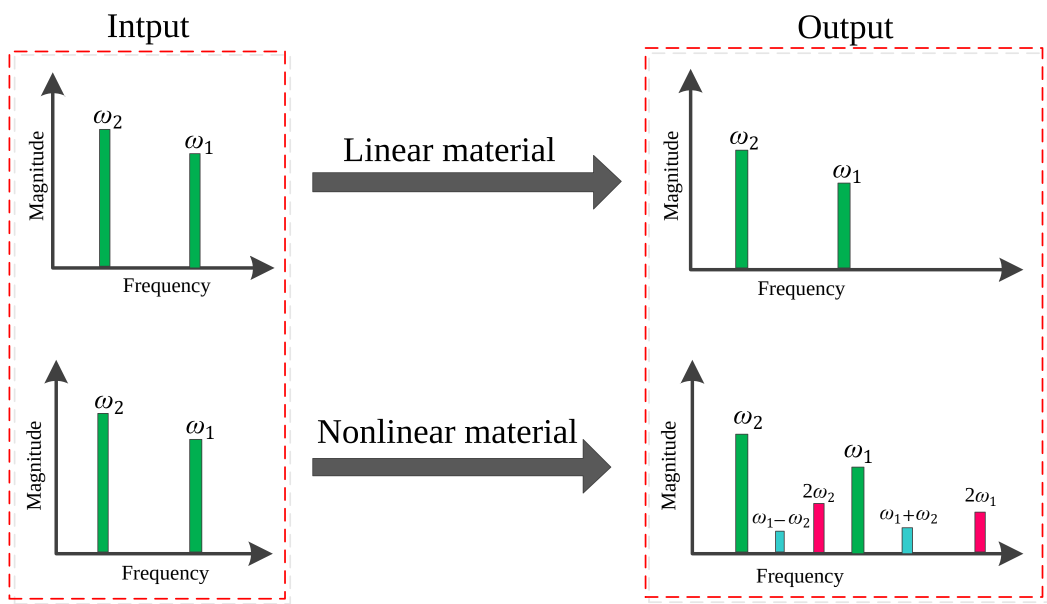

Figure 2.2 Illustration of sideband peak generation

2.3. Proof of HHG and SPG for General case

When a nonlinear material is excited by a harmonic wave with a single frequency f_i, the displacement field u_i within the material can be written as:

$$u_i(x,t) = A_i(x)\sin(\omega_i t) + B_i(x)\cos(\omega_i t) \tag{9}$$

Where $\omega_i = 2\pi f_i$ is angular frequency.

Considering a set of frequencies $\omega_1 > \omega_2 > \cdots \omega_i \cdots > \omega_N$, the total displacement field can be expressed as:

$$u(x,t) = \sum_{i=1}^{N} u_i(x,t) = \sum_{i=1}^{N} [A_i(x)\sin(\omega_i t) + B_i(x)\cos(\omega_i t)]$$

$$= \frac{1}{2}\sum_{i=1}^{N}\left\{[B_i(x) - jA_i(x)]e^{j\omega_i t} + [B_i(x) + jA_i(x)]e^{-j\omega_i t}\right\} \tag{10}$$

Let $\alpha_i = \frac{1}{2}[B_i(x) - jA_i(x)]$, and $\beta_i = \frac{1}{2}[B_i(x) + jA_i(x)]$, then:

$$u(x,t) = \sum_{i=1}^{N} \left(\alpha_i e^{j\omega_i t} + \beta_i e^{-j\omega_i t} \right) \tag{11}$$

And thus,

$$\varepsilon(x,t) = \frac{\partial u(x,t)}{\partial x} = \sum_{i=1}^{N} \left(\alpha_i' e^{j\omega_i t} + \beta_i' e^{-j\omega_i t} \right) \tag{12}$$

For cubic stress-strain relation, the harmonic stress field is formulated as follows:

$$\sigma(x,t) = E_0 \varepsilon(x,t) - E_1 \varepsilon^2(x,t) - E_2 \varepsilon^3(x,t) \tag{13}$$

Substituting Eq. 12 into Eq. 13 yields,

$$\sigma(x,t) = E_0 \sum_{i=1}^{N} (\alpha_i' e^{j\omega_i t} + \beta_i' e^{-j\omega_i t}) - E_1 \left[\sum_{i=1}^{N} (\alpha_i' e^{j\omega_i t} + \beta_i' e^{-j\omega_i t}) \right]^2 - E_2 \left[\sum_{i=1}^{N} (\alpha_i' e^{j\omega_i t} + \beta_i' e^{-j\omega_i t}) \right]^3 \tag{14}$$

The variable part of the second term could be expressed in an alternative form:

$$\begin{aligned} \left[\sum_{i=1}^{N} \left(\alpha_i' e^{j\omega_i t} + \beta_i' e^{-j\omega_i t} \right) \right]^2 &= \sum_{i=1}^{N} \left[(\alpha_i')^2 e^{j2\omega_i t} + (\beta_i')^2 e^{-j2\omega_i t} \right] + 2 \sum_{i=1}^{N} \alpha_i' \beta_i' \\ &+2 \sum_{1 \le i < k \le N} \left[\alpha_i' \alpha_k' e^{j(\omega_i + \omega_k)t} + \beta_i' \beta_k' e^{-j(\omega_i + \omega_k)t} \right] \\ &+2 \sum_{1 \le i < k \le N} \left[\alpha_i' \beta_k' e^{j(\omega_i - \omega_k)t} + \alpha_k' \beta_i' e^{-j(\omega_i - \omega_k)t} \right] \end{aligned} \tag{15}$$

Similarly, the variable part in the third term could be expressed in the following form:

$$\begin{aligned} \left[\sum_{i=1}^{N} \left(\alpha_i' e^{j\omega_i t} + \beta_i' e^{-j\omega_i t} \right) \right]^3 &= \sum_{i=1}^{N} (\alpha_i'^3 e^{j3\omega_i t} + \beta_i'^3 e^{-j3\omega_i t}) + 3\alpha_i' \beta_i' \sum_{i=1}^{N} \left(\alpha_i' e^{j\omega_i t} + \beta_i' e^{-j\omega_i t} \right) \\ &+3 \sum_{1 \le i < k \le N} \left[\alpha_i'^2 \alpha_k' e^{j(2\omega_i + \omega_k)t} + \beta_i'^2 \beta_k' e^{-j(2\omega_i + \omega_k)t} \right] \\ &+3 \sum_{1 \le i < k \le N} \left[\alpha_i'^2 \beta_k' e^{j(2\omega_i - \omega_k)t} + \alpha_k' \beta_i'^2 e^{-j(2\omega_i - \omega_k)t} \right] \end{aligned}$$

$$+3\sum_{1\le i<k\le N}\left[2\alpha_i'\alpha_k'\beta_i' e^{j\omega_k t}+2\alpha_i'\beta_i'\beta_k' e^{-j\omega_k t}\right]$$

$$+6\sum_{1\le i<k<l\le N}\left[\alpha_i'\alpha_k'\alpha_l' e^{j(\omega_i+\omega_k+\omega_l)t}+\beta_i'\beta_k'\beta_l' e^{-j(\omega_i+\omega_k+\omega_l)t}\right]$$
$$+6\sum_{1\le i<k<l\le N}\left[\alpha_i'\alpha_k'\beta_l' e^{j(\omega_i+\omega_k-\omega_l)t}+\alpha_l'\beta_i'\beta_k' e^{-j(\omega_i+\omega_k-\omega_l)t}\right]$$

$$+6\sum_{1\le i<k<l\le N}\left[\alpha_i'\beta_k'\alpha_l' e^{j(\omega_i-\omega_k+\omega_l)t}+\alpha_k'\beta_i'\beta_l' e^{-j(\omega_i-\omega_k+\omega_l)t}\right]$$

$$+6\sum_{1\le i<k<l\le N}\left[\alpha_i'\beta_k'\beta_l' e^{j(\omega_i-\omega_k-\omega_l)t}+\alpha_k'\alpha_l'\beta_i' e^{-j(\omega_i-\omega_k-\omega_l)t}\right] \quad (16)$$

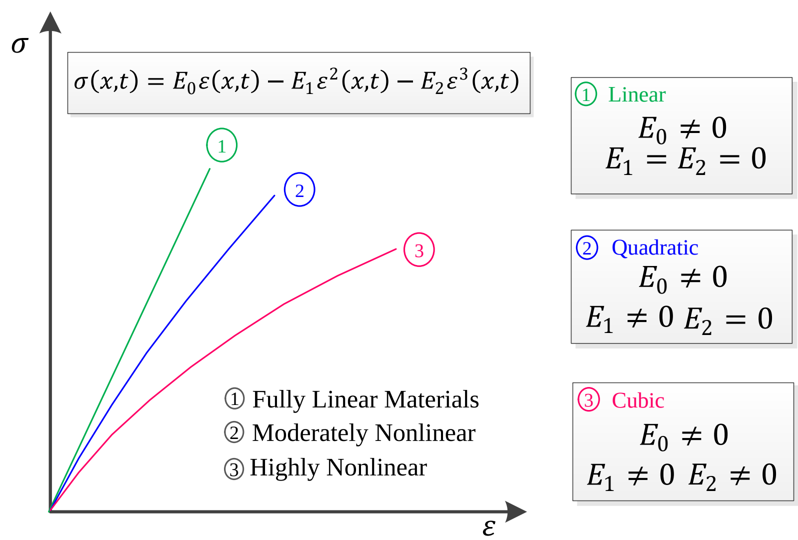

Figure 2.3 Illustration of sideband peak generation

Regarding a classic nonlinear material, its stress-strain relationship can be expanded as follows:

$$\sigma(x,t) = E_0\varepsilon(x,t) - \sum_{i=1}^{N} E_i\varepsilon^{i+1}(x,t) \quad (17)$$

In general, keeping the initial three terms in the above equation is adequate for discussing various levels of nonlinearity in the material's constitutive behavior.

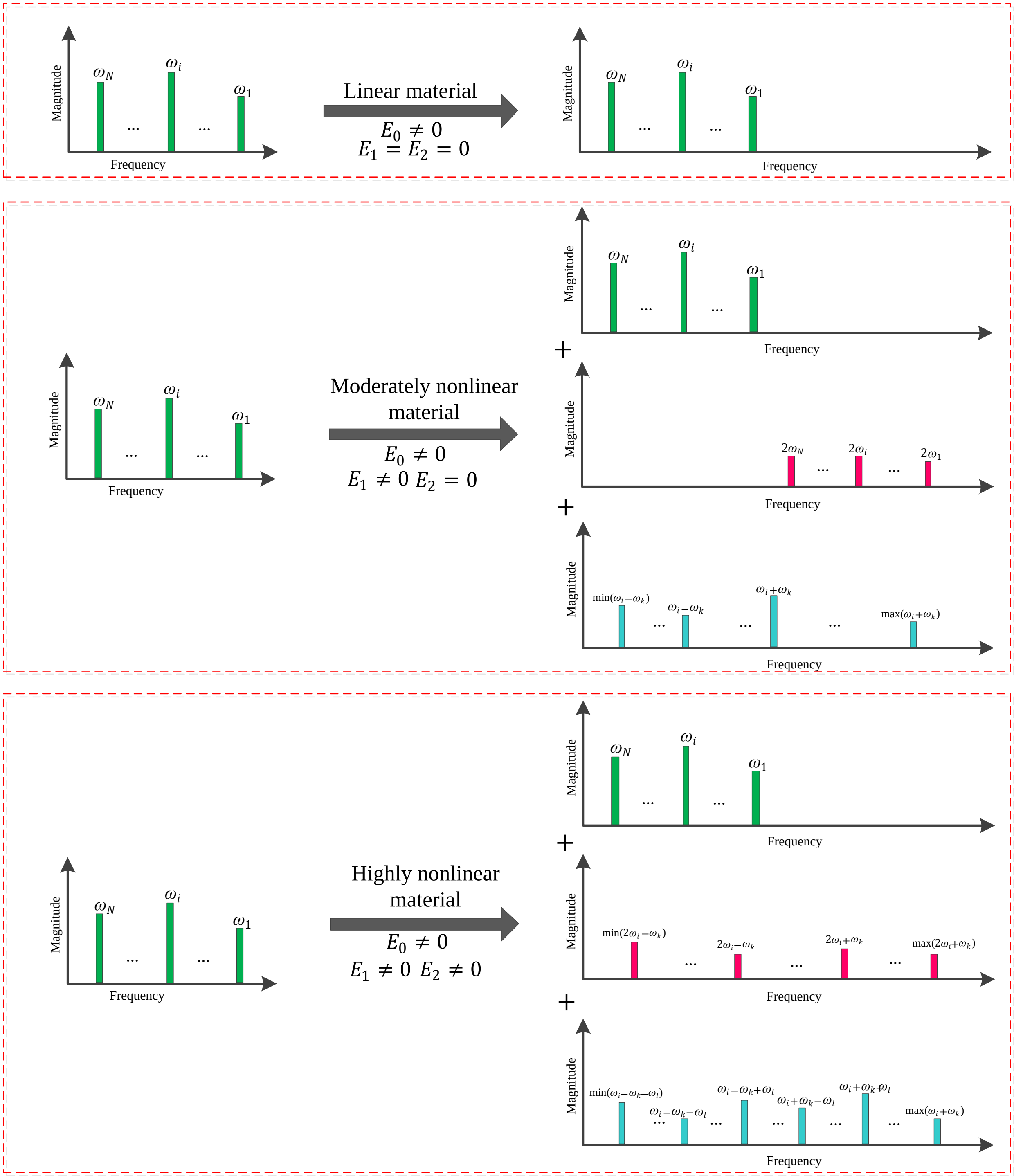

Figure 2.4 Illustration of HHG and SPG for general case.

Thus, as illustrated in Figure 2.3, three distinct scenarios corresponding to the following three categories of materials:

(1.) fully linear materials, i.e., $E_0 \neq 0$, but $E_1 = E_2 = 0$;

(2.) moderately nonlinear materials, i.e., $E_0 \neq 0$, and $E_1 \neq 0$, but $E_2 = 0$;

(3.) highly nonlinear materials, i.e., $E_0 \neq 0$, $E_1 \neq 0$ and $E_3 \neq 0$.

Therefore, for linear materials as well as materials with varying degrees of nonlinearity, the frequency distribution within their response signals demonstrates distinct characteristics, as illustrated in Figure 2.4 and also could be outlined as follows:

(1.) If only E_0 is non-zero among E_0 , E_1, and E_2, thus the material is linear. By retaining only the first term in Eq. (14), results in the response signal exhibiting an identical frequency distribution to the exciting signal, i.e., ω_i (where $i = 1, \dots, N$).

(2.) If $E_0 \neq 0$, and $E_1 \neq 0$, but $E_2 = 0$, the material can be categorized as moderately nonlinear. Alongside the frequencies ω_i (where $i = 1, \dots, N$), harmonic frequencies $2\omega_i$ (where $i = 1, \dots, N$), and modulated wave frequencies $\omega_i \pm \omega_k$ (where $1 \leq i < k \leq N$) are also generated.

(3.) If E_0, E_1, and E_2 are all non-zero, the material exhibits high nonlinearity. Beyond the frequencies outlined in the aforementioned two, numerous additional higher harmonic frequencies and modulated wave frequencies arise, including $3\omega_i$ (where $i = 1, \dots, N$), $2\omega_i \pm \omega_k$ (where $1 \leq i < k \leq N$), as well as $\omega_i + \omega_k + \omega_l$, $\omega_i + \omega_k - \omega_l$, $\omega_i - \omega_k + \omega_l$, and $\omega_i - \omega_k - \omega_l$ (where $1 \leq i < k < l \leq N$).

However, it is worth noting that when damage (such as cracks, voids, corrosion, etc.) occurs in a structure composed of a certain material, although the microscale constitutive behavior of the material itself remains linear, the macroscopic structure exhibits some nonlinear characteristics. In other words, in the damaged areas of the structure, when ultrasonic waves propagate through these regions, their response signals exhibit nonlinear response characteristics such as HHG and SPG derived for nonlinear materials.

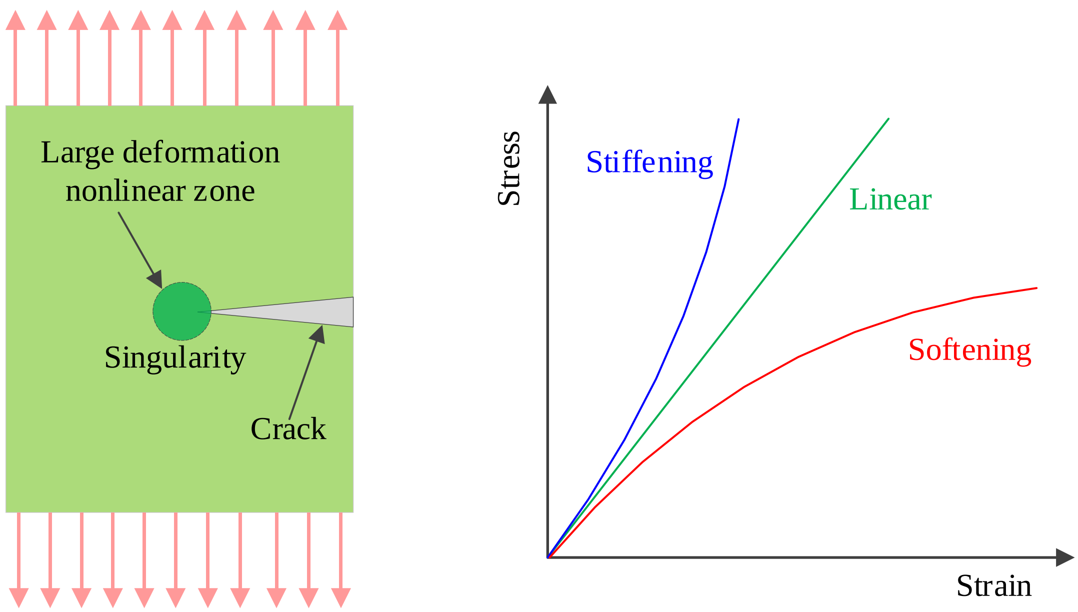

Figure 2.5 Crack tip singularity-induced large deformation and material nonlinearity.

When damage occurs in a material, its constitutive relationship may undergo changes. The presence of damage can introduce nonlinearity into this relationship, as it alters the internal structure of the material, thus affecting its stress-strain response. For instance, the presence of cracks leads to localized stress concentrations, resulting in changes in the strain field around the crack, thereby rendering the overall stress-strain relationship nonlinear. As illustrated in Figure 2.5, the linear elastic approximation holds true only for small deformations. In close proximity to crack tips, material deformation escalates significantly, causing considerable shifts in local elasticity, commonly referred to as material hardening or softening.

3. TRADITIONAL AND NEWLY DEVELOPED NONLINEAR ULTRASONIC TECHNIQUES

Several nonlinear ultrasonic techniques have been developed to assess material nonlinearity. The traditional nonlinear techniques include the Higher Harmonic Generation (HHG) technique, Frequency Modulation (FM) technique (also known as Nonlinear Wave Modulation Spectroscopy or NWMS), Nonlinear Impact Resonant Acoustic Spectroscopy (NIRAS) technique, and the relatively new Sideband Peak Count (SPC) technique. However, in addressing the challenges associated with monitoring initial fatigue cracks in riveted aluminum plates, in this thesis a new nonlinear acoustic technique called the Sideband Intensity (SI) technique is proposed and investigated in this thesis.

3.1. Higher Harmonic Generation (HHG) Technique

The fundamental principle of the HHG technique involves assessing material nonlinearity by generating and measuring higher-order harmonics. In particular, the nonlinear parameter β, which is associated with the amplitudes of the fundamental wave frequency and the second higher harmonic, is employed to quantify material nonlinearity and can be experimentally determined. However, another equivalent parameter $\hat{\beta}$ is more frequently employed since it is directly proportional to β, as defined below:

$$\hat{\beta} = \frac{A_2}{A_1^2} \propto \beta = \frac{8A_2}{A_1^2 k^2 x} \tag{18}$$

where A_1 and A_2 are the amplitudes of fundamental and second harmonic waves, respectively as shown in Figure 3.1. And, k and x in the above equation are the wave number and the wave propagation distance, respectively.

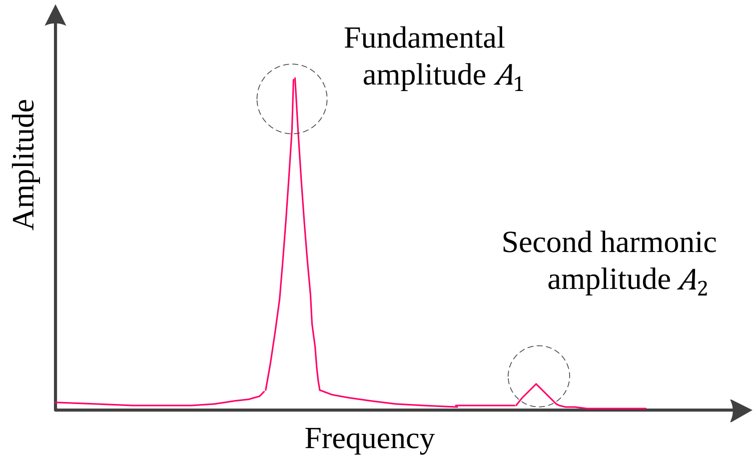

Figure 3.1 Illustration of fundamental and second harmonic amplitudes.

It can be seen that the parameter $\hat{\beta}$ is expressed as the ratio of the second harmonic amplitude A_2 and the square of the fundamental wave amplitude A_1^2 for a fixed wave number and propagation distance. Additionally, the second higher harmonic for longitudinal waves exhibits a cumulative effect as a notable characteristic. To elaborate further, as the propagation path distance increases, the amplitude of the second higher harmonic experiences a linear increase, resulting in an enhancement of the signal-to-noise ratio. This feature remains effective within a certain distance; however, beyond that point, due to material attenuation, the amplitude begins to decrease.

While the HHG technique has a long history and has continuously undergone improvements, it is not devoid of practical limitations. Firstly, it necessitates the preservation of the same wave propagation path, which can be quite challenging, particularly in the presence of boundary reflections and structural heterogeneity. Secondly, the technique demands the application of high voltage to enhance sensitivity, which can pose practical challenges. Thirdly, when applied to waveguides such as plates, pipes, and rods, where wave propagation occurs as guided waves such as generalized Rayleigh waves and Lamb waves, complications arise. The dispersive nature and multi-mode propagation characteristics of guided waves make the generation of higher harmonics a difficult task. To effectively utilize the HHG technique for guided waves, one must ensure the satisfaction of two critical conditions: phase matching and efficient power transfer from the fundamental mode to the second higher harmonic mode.

3.2. Frequency Modulation (FM) Technique

The Frequency Modulation (FM) technique, also known as the Nonlinear Wave Modulation Spectroscopy (NWMS) technique, is centered around the generation of two distinct ultrasound waves of different frequencies, followed by the measurement of their modulation.

In a more specific context, this technique relies on the interaction of two harmonic waves with distinct frequencies ($f_0 < f_1$). Nonlinear parameters can be assessed by examining the amplitude dependence of spectral components, including harmonics ($2f_0, 2f_0, ...$), and intermodulation ($f_1 \pm f_0, f_1 \pm 2f_0, ...$) spectral components. The utilization of FM/NWMS technique relies on the utilization of the equation of state [41].

$$\begin{cases} d\sigma = K d\varepsilon \\ K(\varepsilon, \dot{\varepsilon}, history) = K_0[1 - \beta\varepsilon - \delta\varepsilon^2 - \alpha(\Delta\varepsilon - \varepsilon\, sign(\dot{\varepsilon}))] \end{cases} \tag{19}$$

In the above equations, K_0 is the linear elastic modulus of a material (modulus for small deformation). α is the parameter for material hysteresis. β and δ are the parameters for quadratic and cubic anharmonicity, respectively. ε , $\Delta\varepsilon$ and are $\dot{\varepsilon}$ strain, strain amplitude and strain rate, respectively. The sgn( ) is a symbolic function, and $\mathrm{sgn}(\dot{\varepsilon}) = 1$, if $\dot{\varepsilon} > 0$; $\mathrm{sgn}(\dot{\varepsilon}) = -1$, if $\dot{\varepsilon} < 0$; and $\mathrm{sgn}(\dot{\varepsilon}) = 0$, if $\dot{\varepsilon} = 0$.

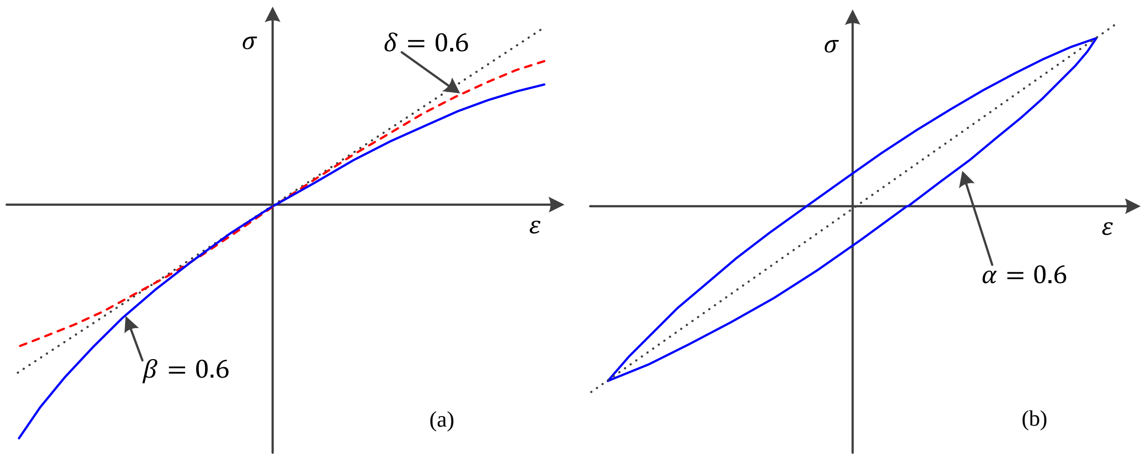

Figure 3.2 Illustration of (a) classical nonlinear, and (b) hysteretic stress strain dependence.

The classic nonlinear components are governed by parameters β and δ, and parameter α corresponds to the nonclassical hysteretic part. The stress-strain relationships for the classical and non-classical components are depicted in Figure 3.2 (a) and (b), respectively. The analysis of FM/NWMS experimental results also depends on the dynamical solution of the above equation subjected to the following excitation $A_0 \cos(\omega_0 t) + A_1 \cos(\omega_1 t)$.

In the case of a material demonstrating classical nonlinearity, the 1st order sidebands (i.e., $f_1 \pm f_0$) are associated with driving amplitudes $C_\beta A_0 A_1$. While, the 2nd order sidebands (i.e., $f_1 \pm 2f_0$) vary with $C_{\beta\delta} A_0^2 A_1$, which indicates that sidebands are quadratic on A_0, and even and odd harmonics appear in the response spectrum. For the specific case involving a purely hysteretic material, there are no 1st order sidebands, and the 2nd order sidebands depend as $C_\alpha A_0^2 A_1$, i.e., quadratic variation for A_0. Thus, only odd harmonics are present in this case.

Compared to the HHG technique, FM/NWMS technique is much more sensitive, and can be applied irrespective of material geometry or the presence of reflecting boundaries and structural inhomogeneity. However, when applying the NWMS/FM technique to guided waves, similar challenges to those encountered in HHG technique arise. Additionally, precise control of the two input wave frequencies is necessary to generate optimal sidebands, which implies the need for narrowband excitation. Besides, the precise selection of two differing frequencies plays a pivotal role when applied to specific structural analyses in the FM/NWMS technique.

3.3. Nonlinear Impact Resonant Acoustic Spectroscopy (NIRAS) Techniques

The NIRAS technique is based on repeatedly subjecting the sample to pulse excitation with varying impact intensities. α_f^{NIRAS} is a parameter that is associated with hysteresis and it corresponds to the shift in resonance frequency. It could be obtained using the following equation based on a set of experimental data.

$$\frac{\tilde{f}_0 - \tilde{f}_i}{\tilde{f}_0} = \alpha_f^{NIRAS} \cdot A_i \tag{20}$$

Where, $\tilde{f}_0$ is the resonance frequency acquired within the linear strain range; $\tilde{f}_i = \max(|Y_i[f]|)$ and $A_i = max_f\ (|Y_i[f]|)$ are the peak frequency and peak amplitude obtained from the *i*-th impact test. It is anticipated that, as the specimen's damage level or the material nonlinearity increases, there will be a corresponding rise in the parameter proportional to hysteresis, which has been denoted as the α_f^{NIRAS}.

Another comparable technique, known as Flipped Accumulative Non-linear Single Impact Resonance Acoustic Spectroscopy (FANSIRAS), can be regarded as a single-impact variation of the NIRAS technique. This technique only requires a single reverberation and digitalized signal $Y_i(n)$ to obtain the non-linearity estimation that is related to the frequency.

The signal processing algorithm is founded on an initial window length equivalent to that of the acquired signals. This window size is then systematically diminished until it reaches the lower bound, as outlined below:

$$Y_{I,}w_p{}^{L_p}(n) = Y_I\ (n) \cdot w_P{}^{L_P}(n - p \cdot M), \quad n \in \{0, \cdots, N-1\}, \text{and } p \in \left\{0, \cdots, \left\lfloor \frac{N}{M} \right\rfloor - 1\right\} \tag{21}$$

Where, $w_P{}^{L_P}(n)$ denotes the rectangular window, which progressively shortens by M samples at each step of the algorithm. The window length varies at each position p, $L_P = N - p \cdot M$. At each window position, the time segment of the impact signal contained within the p-th window, i.e., $Y_{I,}w_p{}^{L_p}(n)$, is subject to a frequency domain transformation. Figures 3.3 (a) and (b) present the graphical depictions of the windowing process in time and frequency domains, respectively.

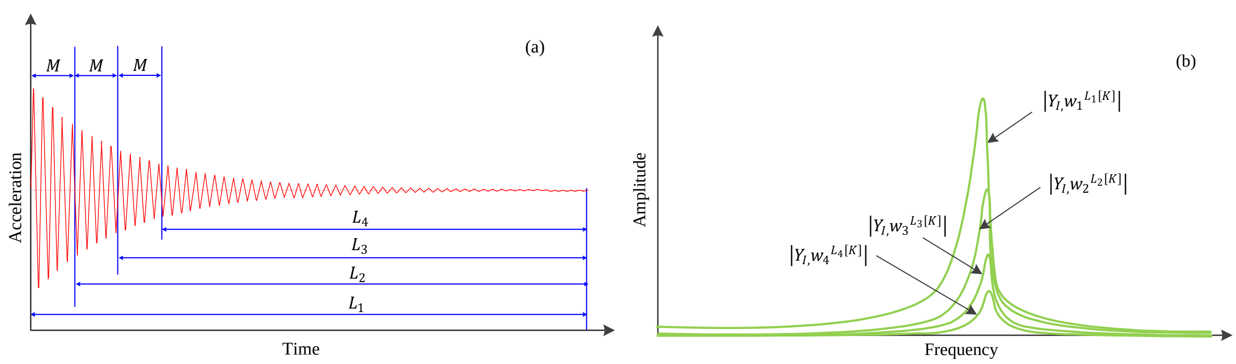

Figure 3.3 FANSIRAS windowing process in (a) time domain, and (b) frequency domain.

Then, the hysteresis parameter $\alpha_{f,I}^{\text{FANSIRAS}}$ could be evaluated through linear fitting as used in the NIRAS technique but reformulated based on the current variables in alignment with the FANSIRAS technique, as demonstrated by the following equation:

$$\frac{\tilde{f}_{I,0} - \tilde{f}_{I,p}}{\tilde{f}_{I,0}} = \alpha_{f,I}^{\text{FANSIRAS}} \cdot A_{I,p} \tag{22}$$

Where, $\tilde{f}_{I,0}$ is the approximation for the resonance frequency in the linear regime associated with the reverberation signal $Y_I(n)$. $\tilde{f}_{I,p} = \max\left(\left|Y_{I,}w_p{}^{L_p}[f]\right|\right)$ and $A_i = max_f\left(\left|Y_{I,}w_p{}^{L_p}[f]\right|\right)$ are the peak frequency and peak amplitude related to the signal segment within the *p*-th window.

3.4. Sideband Peak Count (SPC) Based Techniques

The derivation in chapter 2 shows that material nonlinearity can distort propagating elastic waves, generating higher order harmonics and modulating waves. Thus, materials with higher degrees of nonlinearity tend to generate more sideband peaks, which include all peaks corresponding to the higher harmonic frequencies and modulating wave frequencies. Since the sidebands appear in the spectrum are closely related to the materials' nonlinearity, the nonlinearity characteristics of a material can be quantified by counting the number of these sideband peaks [34].

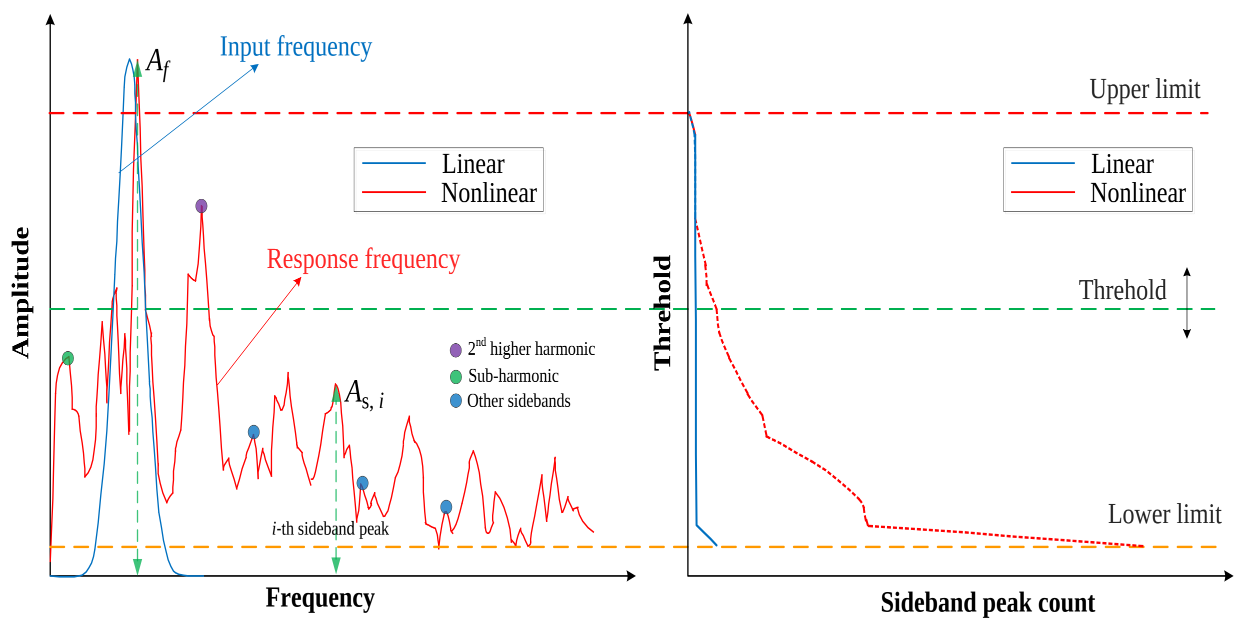

Figure 3. 4 Illustration of the SPC technique.

The SPC technique involves counting the number of sideband peak beyond a certain threshold, with the upper and lower thresholds are determined based on the actual signal-to-noise ratio and the amplitudes of the sideband peaks, as depicted on the left side of Figure 3.4. By plotting the number of counted sideband peaks against their corresponding thresholds, the resulting SPC curve is generated. The SPC curves for nonlinear materials, tend to exceed that of linear materials, as illustrated on the right side of Figure 3.4.

The SPC technique involves counting the number of sideband peak beyond a certain threshold, with the upper and lower thresholds are determined based on the actual signal-to-noise ratio and the amplitudes of the sideband peaks, as depicted on the left side of Figure 3.4. By plotting the number of counted sideband peaks against their corresponding thresholds, the resulting SPC curve is generated. The SPC curves for nonlinear materials, tend to exceed that of linear materials, as illustrated on the right side of Figure 3.4.

As previously mentioned, the SPC curve illustrates how the peak count changes when the threshold value is altered within a designated range, spanning from a lower limit to a upper limit. This variation can be quantitatively described using the SPC value defined below:

$$SPC(LL, UL, T) = \frac{N(T)-N(UL)}{N(LL)-N(UL)}, \qquad (LL \leq T \leq UL) \tag{23}$$

Where, $SPC(T, LL, UL)$ is a function of LL (lower limit), UL (upper limit), and T (threshold) and $N(\,)$ is the counting function that calculates the number of peaks above a certain threshold. Typically, SPC-I is more commonly utilized to assess the nonlinearity of a material. The SPC-Index (SPC-I), obtained by averaging the peak values from the SPC curve [35]:

$$SPC\text{-}I(D) = Average(SPC(LL, UL, T)), \qquad (LL \leq T \leq UL) \tag{24}$$

Where, D represents the count of divisions or the number of threshold lines applied between LL and UL. In most cases, it is recommended to use at least 20 divisions (D). The UL is typically set to 100% of the highest peak value, and the LL is usually positioned above the noise level observed in the received signal.

Another alternative index derived from the sideband peaks is referred to as the sideband peak intensity (SPI), defined as follows [48].

$$\mathrm{SPI} = \sum A_{\mathrm{s},\, i} / A_f \tag{25}$$

Where, $A_{\mathrm{s},\, i}$ and A_f denote the amplitude of the i-th sideband peak and the fundamental peak, respectively as shown on the left side of Fig. 3.4. In contrast to the need for setting three parameters (i.e., upper limit, lower limit and threshold) for computing SPC-I, the calculation of the SPI does not rely on any parameter settings.

From the given definitions of SPC-I and SPI, it could be seen that for a specific threshold value SPC solely counts sideband peaks without taking peak amplitude into account. However, SPC-I indirectly takes into account the peak amplitude since the stronger peak is counted multiple times (for many threshold values) but weaker peaks are counted for only a few times. SPI involves locating these sideband peaks and summing their amplitudes, which is equivalent to simultaneously considering the influence of both the number and amplitude of the sideband peaks. Since the excitation signal's frequency is continuous, it gives rise to a continuous stream of additional harmonic frequencies and modulating wave frequencies on the sideband. Some of these frequencies might overlap, without actually forming distinct sideband peaks in the frequency spectrum. To address this issue the following new technique is proposed in this thesis.

3.5. Sideband intensity index (SII)

The proposed sideband intensity index (SII) is a technique that analyzes the signal's energy across various frequencies. This index can thoroughly incorporate the effects of all harmonic frequencies and modulating wave frequencies generated within the sideband region. It also dispenses with the necessity for several parameters (such as upper limit, lower limit, and threshold), and thus requiring no variables for control.

According to the Parseval's theorem, the energy of a signal in the time domain should be equal to the energy in its corresponding frequency domain [49].

$$E = \int |u(t)|^2 \, dt = \frac{1}{2\pi} \int \left| U(e^{i\omega}) \right|^2 \, d\omega \tag{26}$$

Where, E is the energy of the signal; $u(t)$ is the signal in time domain; $U(\omega)$ is the signal in frequency domain; t and ω are the time and frequency, respectively.

Thus, the sideband intensity index (SII) could be defined as the ratio of the energy associated with sideband frequency components in the signal to the total energy of the signal, as indicated by the following equation.

$$SII = \frac{E_{LSB} + E_{USB}}{E} = \frac{\int_0^{\omega_{\mathrm{lower}}} |U(\omega)|^2 d\omega + \int_{\omega_{\mathrm{upper}}}^{\omega_{\max}} |U(\omega)|^2 d\omega}{\int_0^{\omega_{\max}} |U(\omega)|^2 d\omega} \tag{27}$$

Where, E_{LSB} and E_{USB} refer to the energy in the lower-sideband and the upper-sideband, respectively; ω_{lower} and ω_{upper} correspond to the cutoff frequency of the lower-sideband and the starting frequency of the upper-sideband, respectively. Meanwhile, $\omega_{\max}$ represents the maximum frequency present in the signal.

4. SAMPLE DESCRIPTION AND EXPERIMENTAL METHODS

The experiment comprises two main components. Firstly, fatigue loading is conducted on a riveted aluminum plate, with the objective of inducing the initiation and propagation of cracks within the rivet joint region. These cracks are challenging to identify through visual inspection alone. Subsequently, ultrasound testing is performed on the rivet-joined aluminum plates with induced fatigue cracks. Specimen details and the experimental setup and methods are outlined below.

4.1. Test specimen

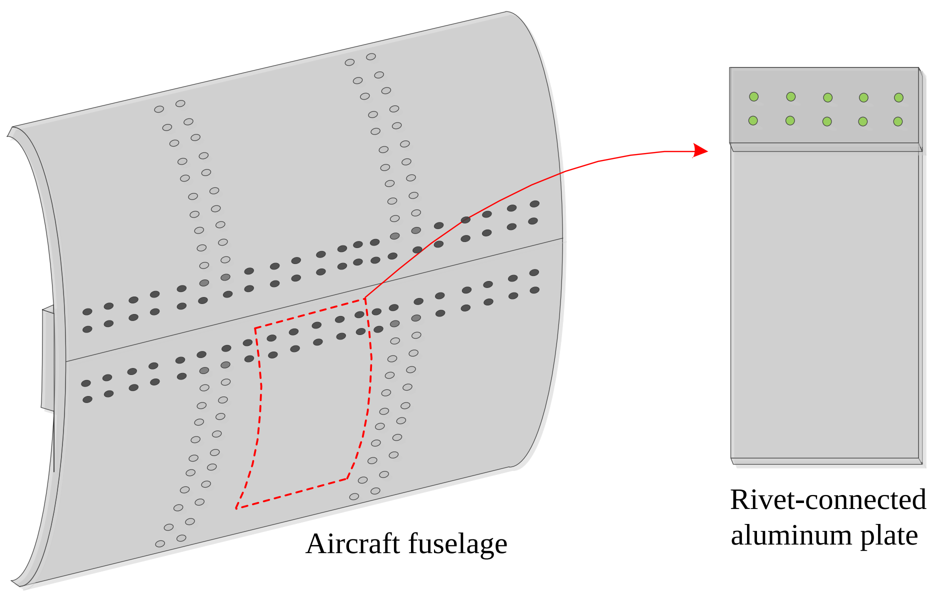

Figure 4. 1 Sampling feature-representative region from aircraft skin.

The prototype of test specimen is selected from the critical feature area on the aircraft fuselage skin, as shown in Figure 4.1. The test sample plate is fabricated from two aerospace aluminum sheets with thicknesses of 0.8 mm and 2.0 mm, respectively. Both of these sheets are composed of Al-alloy 2024 (Al2024-T3). These sheets are of equal width but different lengths and are joined together using rivets. In addition, there is an adhesive layer between the two aluminum sheets at the riveted joint region. The head and shank of the rivets have a diameter of 6 mm and 5 mm, respectively. Details about all dimensions of the front and back side of the specimen are shown in Figure 4.2. Three PZT sensors were arranged vertically on the left side of the specimen front, while two were arranged on the right side. During the test, the 3 PZTs on the left side were used as exciters and the 2 PZTs on the right side were used as receivers.

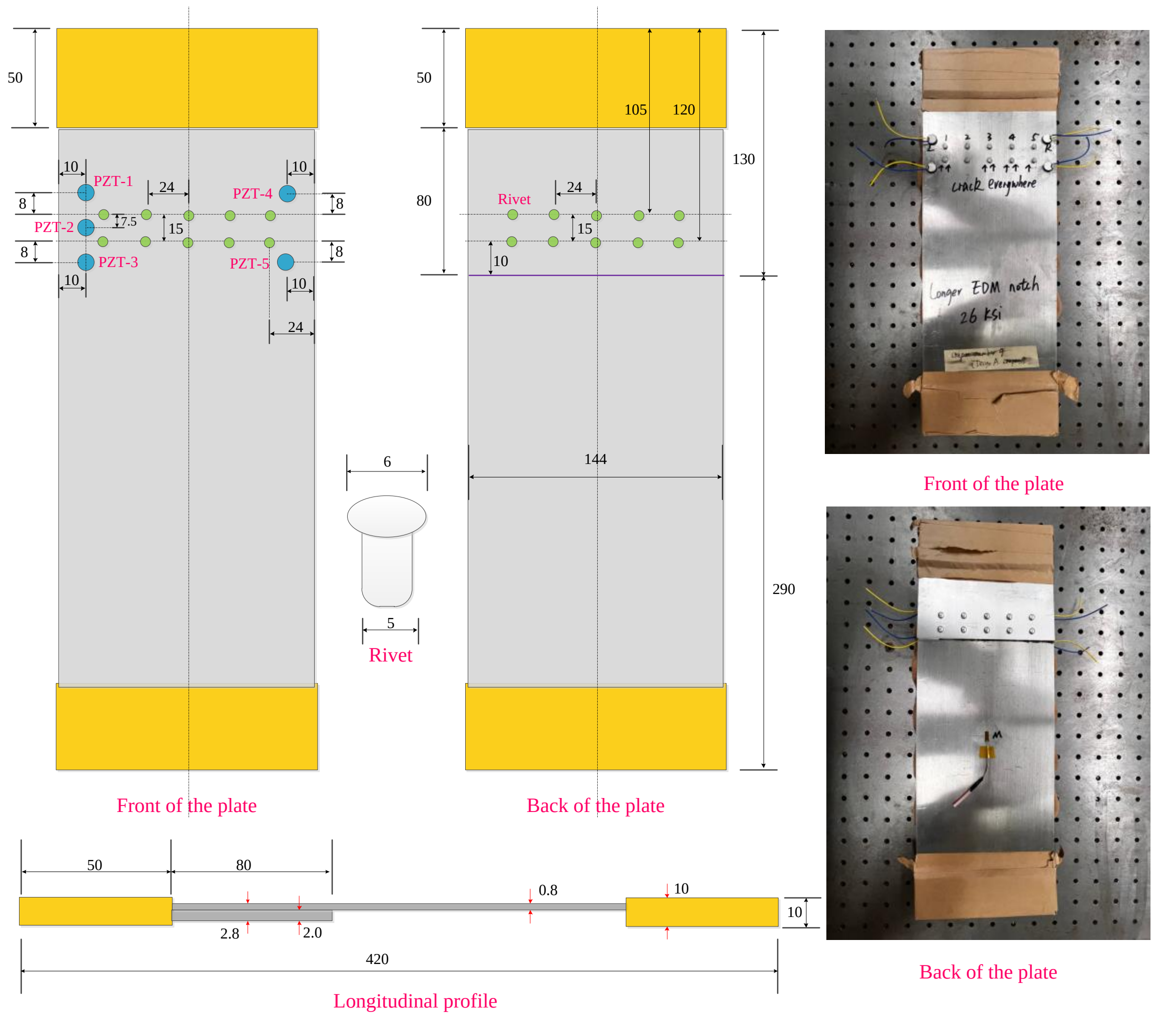

Figure 4. 2 Sample dimensions.

4.2. Fatigue test

In order to simulate the fatigue cracks generated in the rivet area of rivet-jointed aluminum plates under cyclic loading, a fatigue test was conducted on the specimens initially. The fatigue test was conducted at the Boeing Corporation, and here, only a brief overview of the fatigue testing is provided.

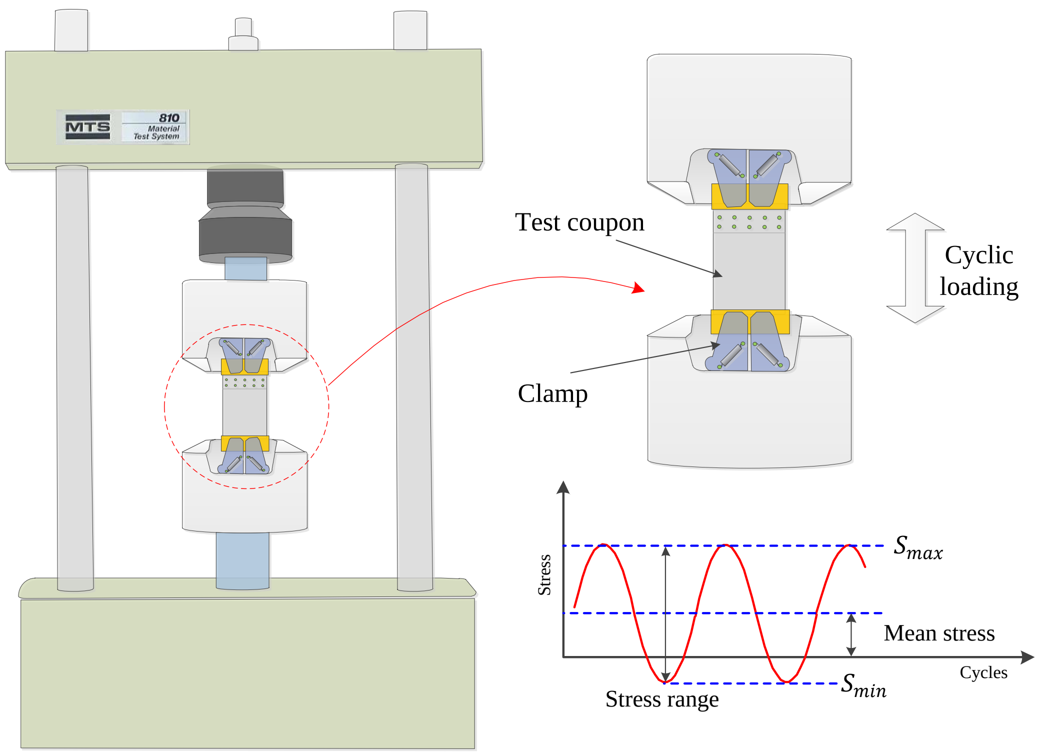

Figure 4. 3 Illustration of the setup of fatigue test.

Figure 4.3 depicts the schematic diagram of the fatigue test setup and the cyclic loading procedure. During the fatigue test, the two ends of a test coupon were clamped vertically on the fatigue loading system. As there are no existing cracks in the structure, a sequence of sinusoidal loading cycles is employed to initiate the fatigue crack. This loading regimen comprises specific sinusoidal cycles characterized by defined peak values and stress ratios, continuing until cracks are detected around the rivet holes.

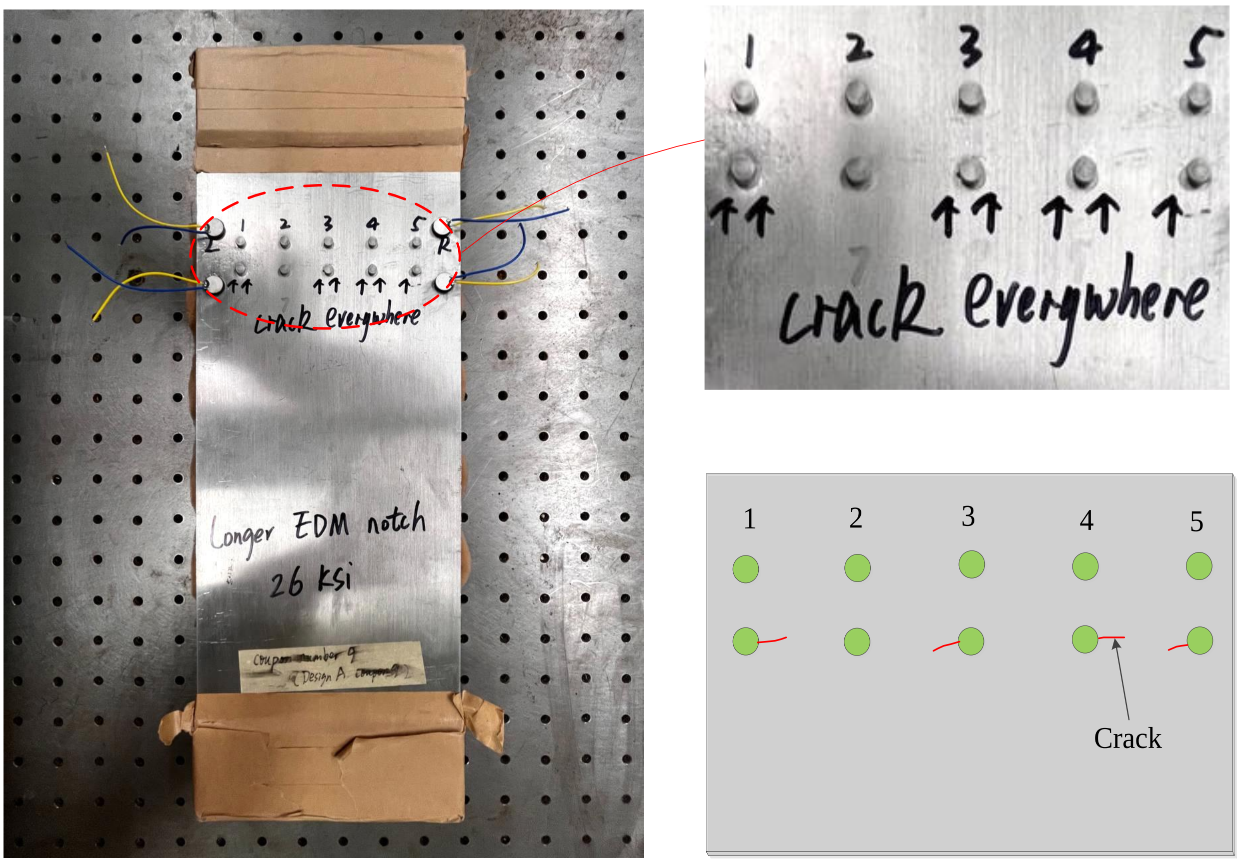

Figure 4. 4 The crack distribution on the test coupon after fatigue test.

Following several loading cycles, the fatigue crack emerged around the rivet holes beneath the 1st, 3rd, 4th, and 5th rivet columns, as shown in Figure 4.4. However, no noticeable cracks were observed along the edges of the two rivet holes above and below the 2nd column. It is also noteworthy that no cracks appeared in the vicinity of the row of rivets located on the upper side. This is because the lower row of rivets is closer to the boundary or edge of a plate. Therefore, relative to the upper row of rivets, it is more likely to undergo deformation and typically experiences higher stress or load, making it more susceptible to fatigue cracking.

4.3. Ultrasonic testing

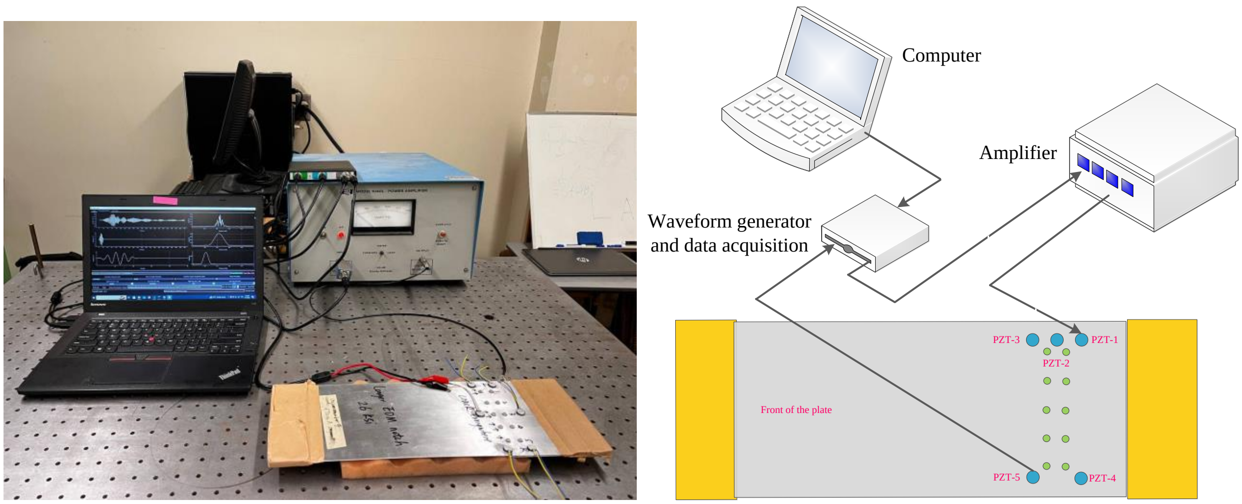

Figure 4. 5 Photograph and Diagram of Ultrasonic Testing Setup.

Ultrasonic testing system used in this study contains computer, computer-controlled testing instrument, power amplifier, and the Piezoelectric (PZT) transducers or sensors, as shown in Figure 4.5. The computer-controlled testing instrument integrated the following functions: arbitrary waveform generator, data acquisition and oscilloscope. During the test, a tone burst was first generated and amplified by a power amplifier and then sent to a PZT transducer to excite Lamb waves in the test sample plate. Another PZT sensor on the other side picks up the arrived wave signals and it is recorded by the data acquisition system.

The Piezoelectric (PZT) transducers used in this study are 10 mm in diameter and 1 mm thick PZT disks, which were employed for generating ultrasonic waves and receiving waves on the tested aluminum plate. This implies that the mentioned PZT disks are utilized for both actuation and reception purposes. The fundamental resonance frequencies for the PZT disk is 215 kHz. A two-component epoxy glue was utilized for bonding the transducers to the aluminum alloy plates.

4.4. Excitation signal

The propagation of planar ultrasonic guided waves is intricately governed by the fundamental principles encapsulated within Navier's equation of motion, which mathematically describes the dynamic behavior of the waves, and the boundary conditions that define the interaction of these waves with their surroundings. Specifically, these boundary conditions are characterized by the absence of traction forces, creating traction-free surfaces that influence the way these guided waves travel and interact with their medium. This complex interplay between the governing equation and the boundary conditions gives rise to a rich and nuanced dispersion behavior, where the phase and group velocities of these waves exhibit intricate dependencies on the excitation frequency. Understanding these dispersion characteristics is crucial for optimizing and harnessing the potential of planar ultrasonic guided waves in various applications, such as non-destructive testing, structural health monitoring, and material characterization.

The resultant dispersion relations provide a valuable insight into the intricate interplay between phase and group velocities, elucidating their intricate dependence on the excitation frequency across various modes. These dispersion curves serve as a roadmap, delineating the dynamic changes in velocities as a function of the excitation frequency. In doing so, they unveil the distinct wave propagation characteristics unique to each mode.

Within the context of Lamb waves, which are typically composed of a composite of multiple modes, we find waves traversing through a solid plate. These modes can be conveniently categorized as either symmetric (S) or anti-symmetric (A). Calculating their dispersion relations within a homogeneous and isotropic plate calls for the well-established Rayleigh-Lamb frequency relations—a foundational tool within the realm of wave propagation analysis. These relations not only provide a means to unravel the underlying physics of wave behavior but also offer crucial insights into the dynamic interplay of symmetric (S) and anti-symmetric (A) modes within this intricate wave propagation framework.

For symmetric modes:

$$\frac{\tan(qh)}{\tan(ph)} = \frac{4k^2pq}{(q^2-k^2)^2}$$

While for antisymmetric modes:

$$\frac{\tan(qh)}{\tan(ph)} = \frac{(q^2-k^2)}{4k^2pq}$$

Where, $p^2 = \frac{\omega^2}{c_L^2} - k^2$; $q^2 = \frac{\omega^2}{c_T^2} - k^2$; $k = \frac{\omega}{c_P}$, and h, k, ω, c_L, c_T, c_P denote plate thickness, wavenumber, circular frequency, longitudinal wave velocity, transverse wave velocity and phase velocity, respectively.

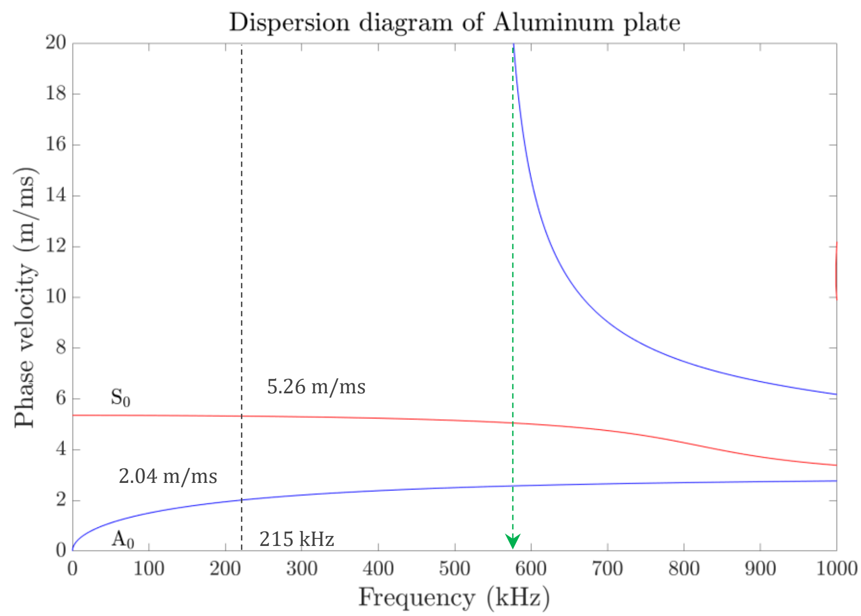

(a) phase velocity.

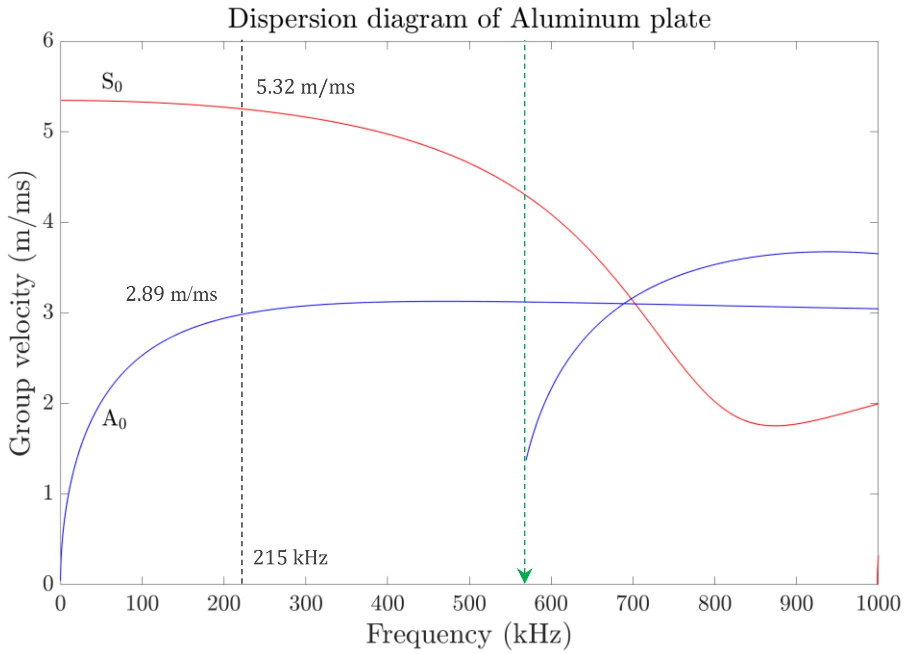

(b) group velocity.

Figure 4.6 Disperse curves for 2.8mm aluminum plate:(a) phase velocity and (b) group velocity.

The resulting dispersion relations offer a valuable understanding of the relationship between phase and group velocities and their dependence on the excitation frequency for various modes. These dispersion curves delineate how the velocities change as a function of the frequency of excitation, thereby revealing the unique wave propagation characteristics associated with each mode.

The dispersion curves revealed that different modes have different phase velocities and group velocities, as shown in Figure 4.6. Based on the dispersion characteristics of Lamb waves in the specific material being tested, the test protocol design is optimized and the accuracy of the damage detection method can be improved. While practical sensitivity can vary depending on factors such as material properties, the type of damage, and the detection methodology, it is generally considered that the A_0 mode is the most sensitive to internal damages within materials like aluminum plates. Indeed, having fewer excited modes is advantageous for subsequent data analysis in the context of structural health monitoring using Lamb waves. Hence, to prioritize exciting the A_0 mode, one should choose the suitable excitation frequency.

Based on the dispersion curves, the critical frequency for each mode can be determined, as indicated by the vertical lines with arrows on the graph, pointing to the critical frequencies of A_1 mode. When the frequency surpasses this threshold, i.e., approaches 600 kHz, the A_1 mode will be additionally excited. However, it is evident that the central frequency has not yet reached the excitation frequency of the A_1 mode, indicating that the primary excited modes in the experiment are A_0 and S_0. In reality, this is not an absolute rule, and other modes may still be excited. However, it is important to emphasize that the A_0 mode is the predominant component.

From these dispersion curves, it also can be inferred that at the central excitation frequency 215 kHz, the phase velocities for the A_0 and S_0 modes are 2.04 m/ms and 5.26m/ms, respectively. Additionally, the group velocities for these two modes are 2.89 m/ms and 5.32 m/ms, respectively.

In this study, the excitation signal is a 5-cycle sinusoidal toneburst enclosed in a Hanning window with 215 kHz center frequency. This excitation signal can be mathematically expressed as follows:

$$S(t) = w(n)\sin(2\pi f t) \tag{28}$$

Where, $S(t)$ is the excitation signal, $w(n) = \frac{1}{2}\left(1 - \cos\left(\frac{2\pi f t}{n}\right)\right)$ is the Hanning window, *n*=5 is the number of cycles. The waveform for exciting is illustrated in Figure 4.7 (a), it could be seen that a zero-amplitude signal is added to extend the toneburst signal until 5×10^{-3}s at the end. This extension is designed to create a distinct time gap between excitation signals, mitigating any potential overlap and interference. Additionally, the spectrum corresponding to the excitation signal is depicted in Figures 4.7 (b) and (c), representing both normal and logarithmic scales, respectively.

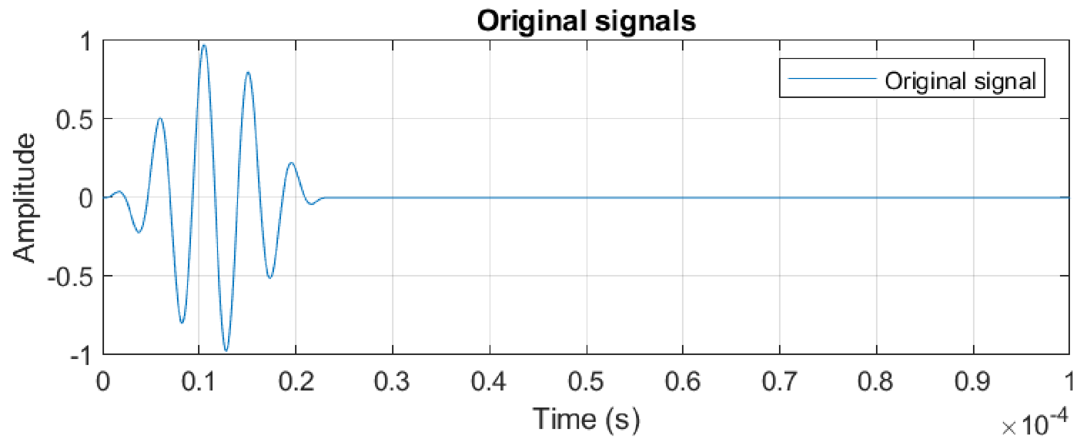

(a) Excitation signal in time domain.

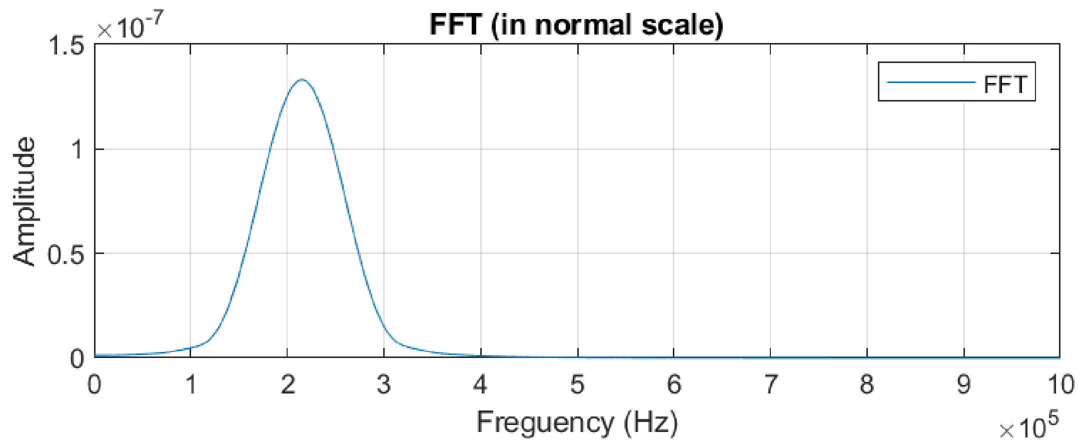

(b) Excitation signal in frequency domain (normal scale).

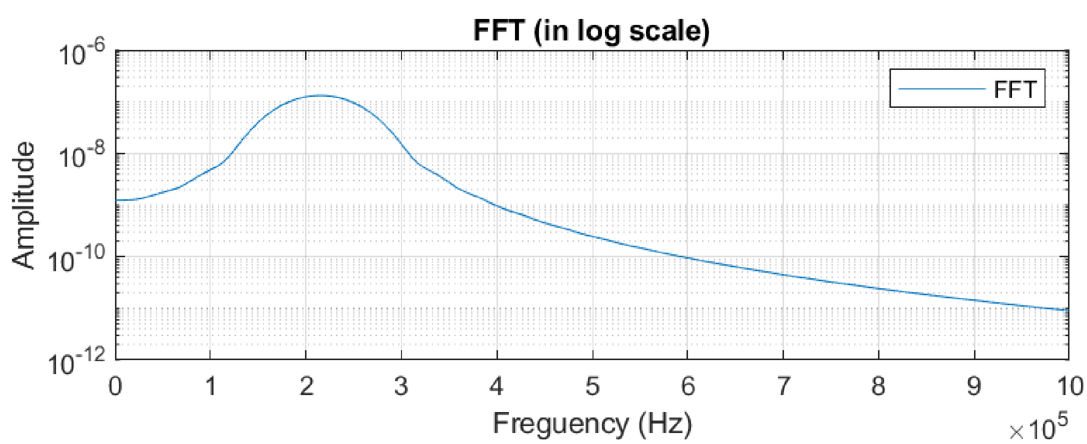

(c) Excitation signal in frequency domain (log scale).

Figure 4.7 Excitation signal: (a) Excitation signal in time domain; (b) Excitation signal in frequency domain (normal scale); and (c) Excitation signal in frequency domain (log scale).

5. TEST RESULTS AND DISCUSSION

In this chapter, the data processing procedure is first meticulously explained, drawing upon the results obtained from a single test. Following this, a broader dataset is employed to conduct a comparative analysis of the existing SPC-I and SPI techniques, along with the SII technique introduced by the authors. This analysis is aimed at facilitating a comprehensive assessment of the performance and effectiveness of these techniques.

5.1. Data Processing and Analysis Flow

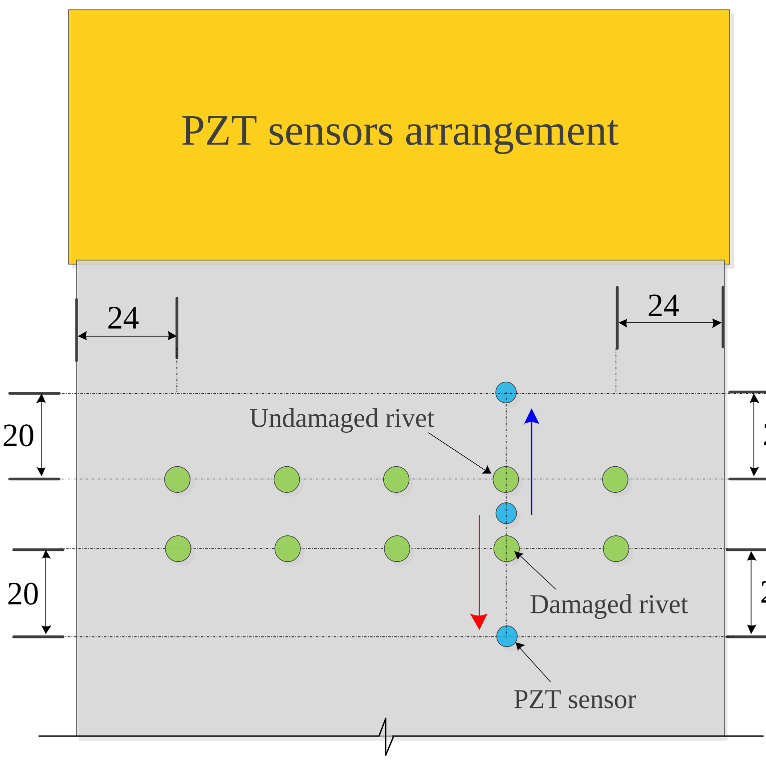

Figure 5.1 The arrangement of the PZT sensors

Here, we have selected two test signals to illustrate the data processing and analysis flow of the test data. These two test signals originate from signals collected by two PZT sensors located on the upper and the lower sides, as shown in Figure 5.1. The upper rivet is undamaged, while the lower rivet contains fatigue cracks. One PZT actuator is positioned between these two rivets. The red and blue arrows in the figure correspond to the propagation paths for damaged and undamaged conditions, respectively.

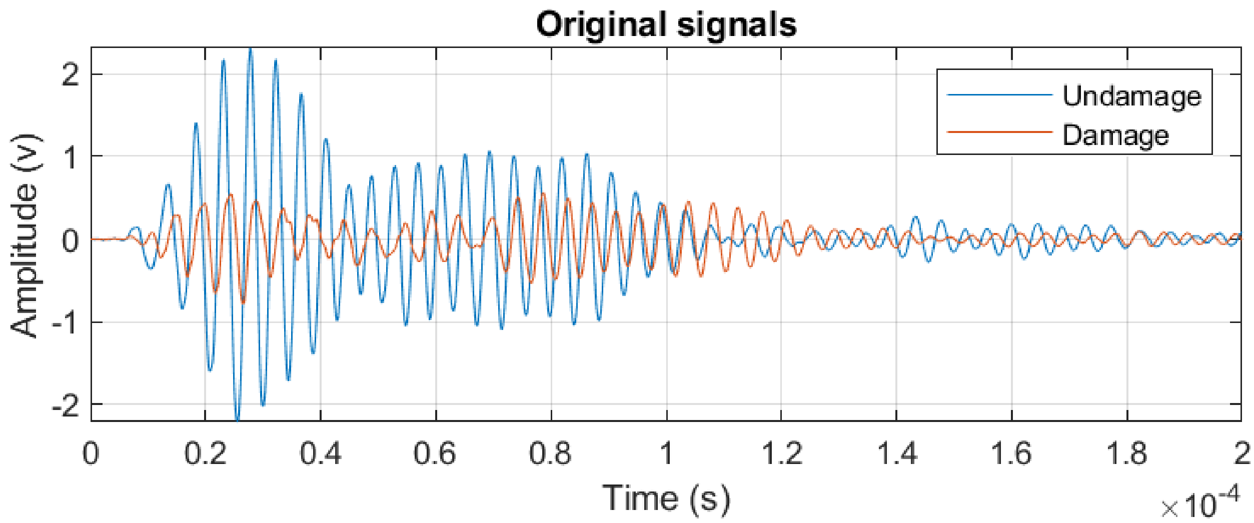

Figure.5.2 Original signals collected by PZT sensors.

The signals collected by the two PZT sensors which are located on the upper and lower sides, are as shown in Figure 5.2. One can observe lower signal amplitudes on the side with a fatigue crack compared to the side that is undamaged because fatigue cracks block some energy from propagating to the receiving sensor.

To comprehensively analyze the spectrum information of received signals, a range of signal processing methods can be employed, such as continuous wavelet transform (CWT) and power spectral density (PSD), each offering its own advantages. Nevertheless, the fast Fourier transform (FFT) stands out as the most straightforward and widely used technique for seamlessly translating signals from the time domain into the frequency domain. Thus, the FFT was adopted in this study to obtain the spectrum of each received signal. The normalized spectra are plotted in both normal and logarithmic scales in Figures 5.3 (a) and (b), respectively.

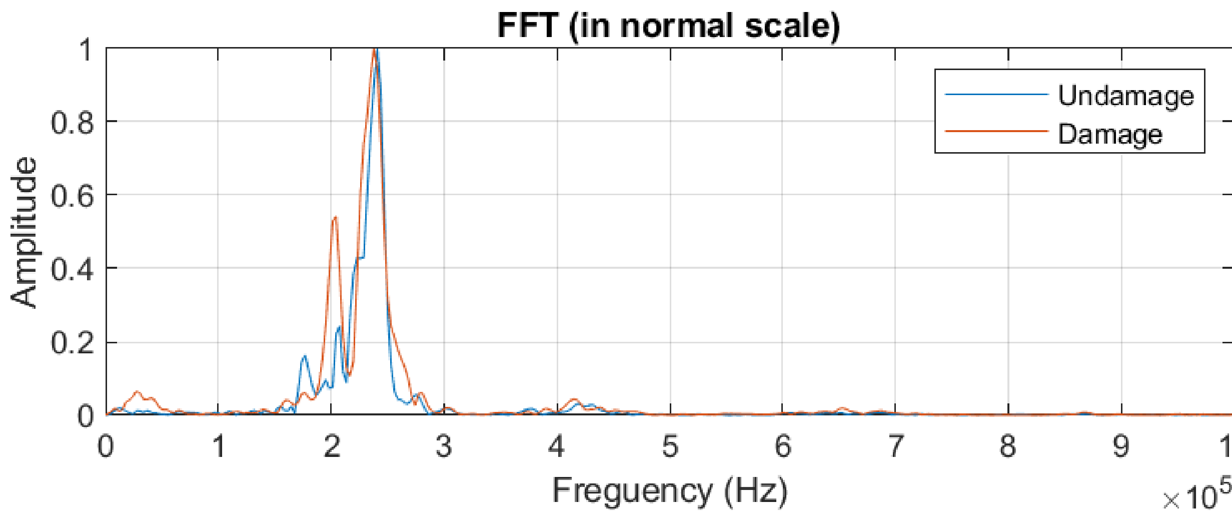

(a) Normal scale.

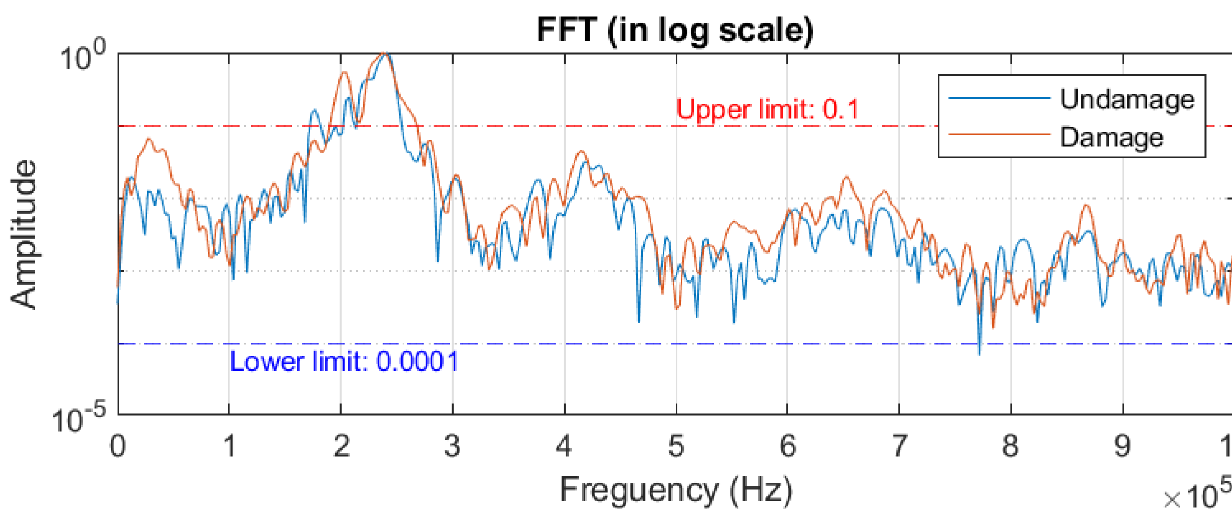

(b) Logarithmic scale.

Figure 5.3 FFTs of the two received signals: (a) Normal scale; and (b) Logarithmic scale.

In the normal scale, some very subtle variations on the spectrum plot may not be easily discernible. Therefore, it is appropriate to depict the spectrum in a logarithmic scale. From the spectrum plotted in a logarithmic scale, it becomes relatively easier to determine reasonable upper and lower limits of the sidebands that are observed away from the central excitation frequency of 215 kHz. The underlying principle is to set the upper and lower limits in a way that effectively encompasses the peaks and dips of the sidebands. For instance, in the case of those two received signals, setting the upper limit to 0.1 and the lower limit to 0.0001 effectively encompasses all the sideband peaks and dips, as indicated by the dashed line in Figure 5.3 (b).

Pseudocode for calculation of SPC and SPI

```
>Start
   Initialize N, SPC, threshold, SPC_index

>For i from 1 to (M - 1) with a step of 2
do the following loop:
      Extract data from FFT and normalize it as FFT_N
      Initialize threshold_temp with N evenly spaced values between
the lower and upper limit, i.e., 0.0001 and 0.1

>Initialize SPC_temp and peak_sum as arrays of zeros

>For j from 1 to the length of threshold_temp
do the following loop:
       Use the findpeaks function to locate peaks in FFT_N with a
minimum peak height of threshold_temp(j)
         Calculate and record the number of peaks in SPC_temp(j)
         Calculate and record the sum of peak heights in peak_sum(j)
      End of j loop

>Store threshold_temp in the i-th and (i+1)-th columns of SPI
      Store peak_sum in the (i+1)-th column of SPI
      Calculate SPI_index((i+1)/2,1)

>Store threshold_temp in the i-th and (i+1)-th columns of SPC
      Store SPC_temp in the (i+1)-th column of SPC
      Calculate SPC_index((i+1)/2,1)

   End of i loop
End
```

The provided pseudocode describes the computation of the SPC curve and SPC index. In this context, "FFT" refers to the results obtained from the Fast Fourier Transform (FFT) calculation. All received signals are subjected to FFT, and the resulting data is stored in an array named "FFT." The variable "*M*" represents the length of a single column within this array.

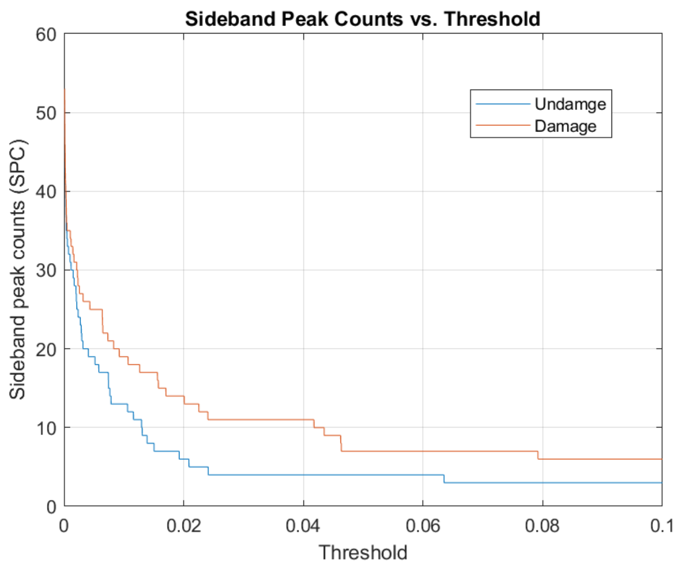

Figure 5.4 Sideband peak count (SPC) vs. threshold curve.

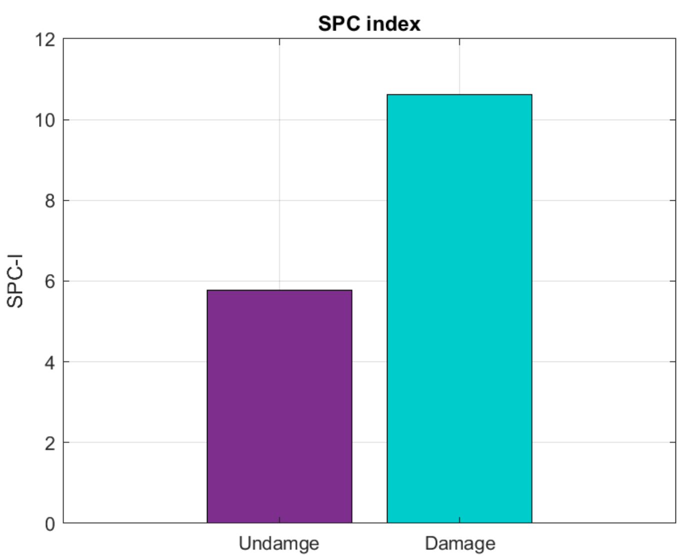

Figure 5.5 Sideband peak count - index (SPC-I) plot.

The SPC curves and SPC-I variations [33, 42, 44] are shown in Figures 5.4 and 5.5, respectively. It is evident that the SPC curve corresponding to the damaged rivet lies well above the SPC curve associated with the undamaged rivet. Furthermore, the SPC index for the damaged signal exceeds 10, whereas the SPC index for the undamaged signal remains below 6. Consequently, both the SPC curve and the SPC index serve as effective tools for identifying rivets with fatigue cracks. It should be mentioned that SPC and SPC-I are measures of the nonlinear response of the material. Therefore, it implies that fatigue cracks introduce nonlinearity to the material response. This is because as the ultrasonic waves pass through the crack the crack surfaces open and close. This phenomenon is known as clapping or breathing of cracks. The local stiffness changes with time as the cracks breathe and it gives rise to the nonlinear response of the material.

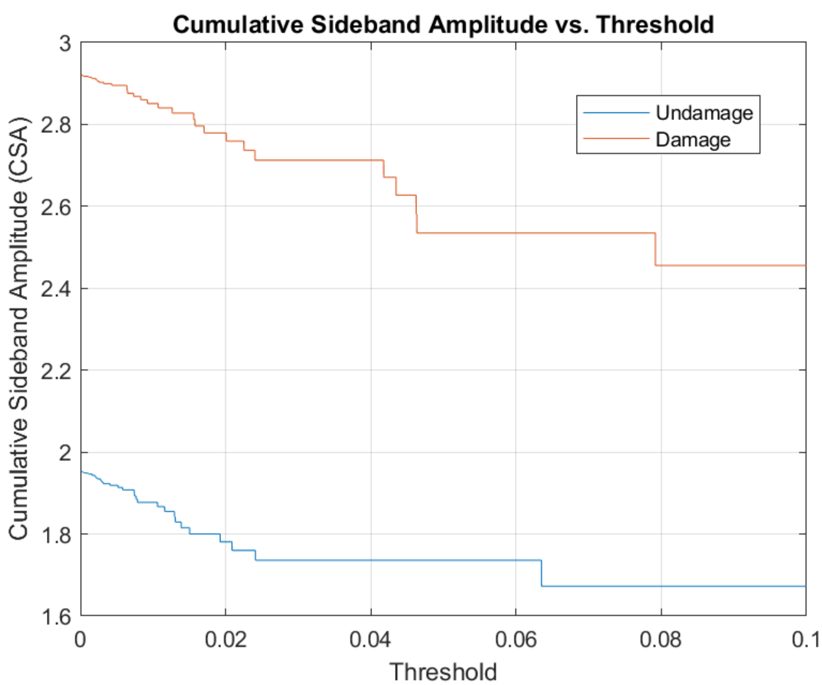

Figure 5.6 Cumulative sideband amplitude vs. threshold curve.

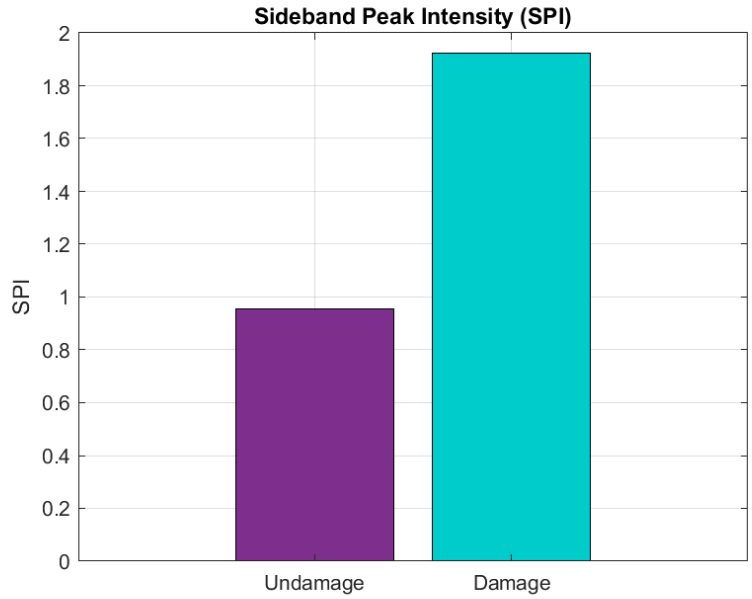

Figure 5.7 Sideband peak intensity (SPI) plot.

The SPI technique developed by Park et al. [48] can be considered as a variation of the SPC method, sharing similarities in algorithmic approaches with some differences in specific steps. The pseudocode provided above for SPC computation also encompasses the calculation of SPI.

Corresponding results for the SPI technique, including the Cumulative Sideband Amplitude vs. Threshold Curve and SPI Index, are shown in Figures.5.6 and 5.7. One can see in the cumulative sideband amplitude versus threshold curve plot, the signals from the the damaged rivet exhibit higher values than the signals from the undamaged rivet. The SPI value of the damaged signal is close to 2, while the SPI value of the undamaged signal remains below 1.

Pseudocode for calculation of SII

```
>Start
   Initialize FFT, integral_value, window_start, window_end, abs_diff1,
abs_diff2, start_index, end_index, cum_start, cum_end, cum_max,
CSPI, SII, alpha

>For each pair of columns 'i' and 'i+1' in FFT data,
   repeat the following steps:
   Extract and normalize data from columns 'i' and 'i+1' into data_temp

   Compute the cumulative energy integral for data_temp and store it in
integral_value

>Set the window start value as window_start and the window end value
as window_end
   Calculate the absolute differences between each data point and
window_start, and find the index with the minimum absolute difference
as start_index
    Calculate the absolute differences between each data point and
window_end, and find the index with the minimum absolute difference
as end_index
    Calculate the cumulative energy curve's start value cum_start, end
value cum_end, and maximum value cum_max
    Calculate the Sideband Intensity Index (SII) as (cum_max -
cum_end) / cum_max
    Calculate alpha as (cum_max - cum_end) / (cum_end - cum_start)

    End of loop for each pair of columns in FFT data
End
```

The provided pseudocode describes the process of calculating the Sideband Intensity Index (SII), which involves cumulatively integrating the spectrum obtained from the Fast Fourier Transform to derive the Cumulative Spectral Energy Curves. Subsequently, it computes the energy associated with the sidebands and center window positions using these curves. Finally, based on the energy distribution at various frequency positions, it determines the SII.

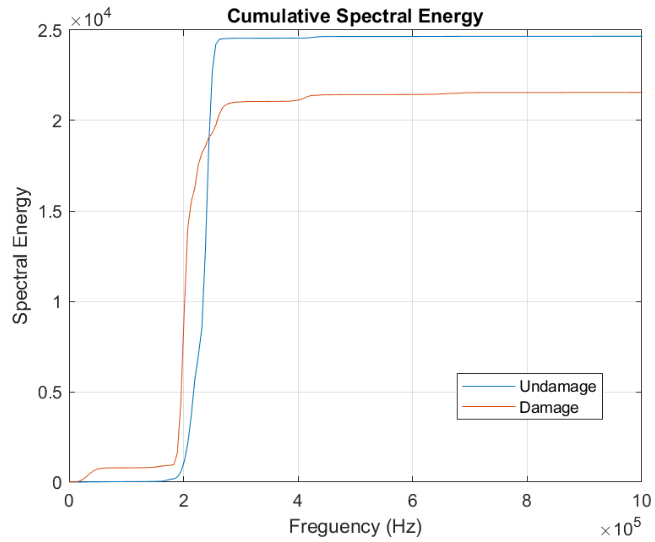

Figure 5.8. Cumulative spectral energy curve.

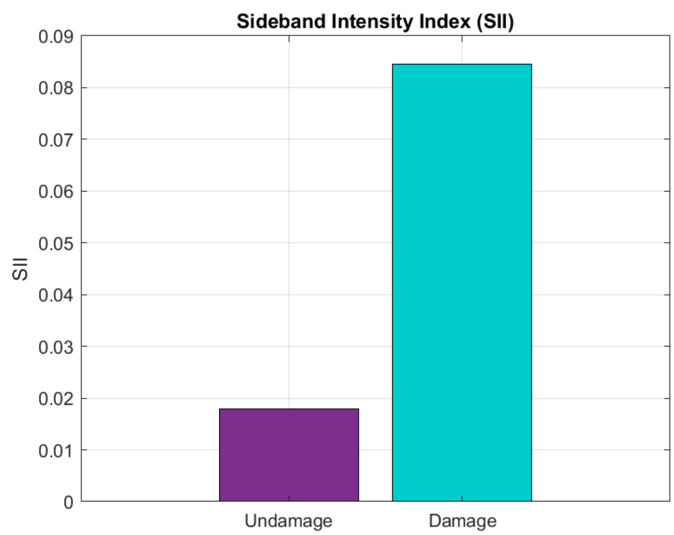

Figure 5.9 Sideband intensity index (SII) plot.

The Cumulative spectral energy curves and SII calculated according to the above algorithm are presented in Figures 5.8 and 5.9, respectively. It is important to note that the spectral energy curves are computed based on a normalized spectrum rather than directly from the FFT-derived spectrum. Consequently, the spectral energy curve associated with the damaged signal may appear lower than that of the undamaged signal. The essence of the SII technique lies in the ratio of spectral energy on the sideband to that at the central window. It is evident that, compared to SPC and SPI indices, the SII shows a higher difference between damaged and undamaged rivets. In fact, in this plot the signal from the damaged rivet exhibits SII value that is eight times higher than that from the undamaged rivet.

5.2. Verification and Analysis via Blind Test Results

In our previous work, we employed two received signals to provide a detailed demonstration of the data processing and analysis workflow. This also served as our initial attempt to validate the effectiveness of the SPC, SPI, and SII techniques in the context of monitoring fatigue cracks in rivet plates.

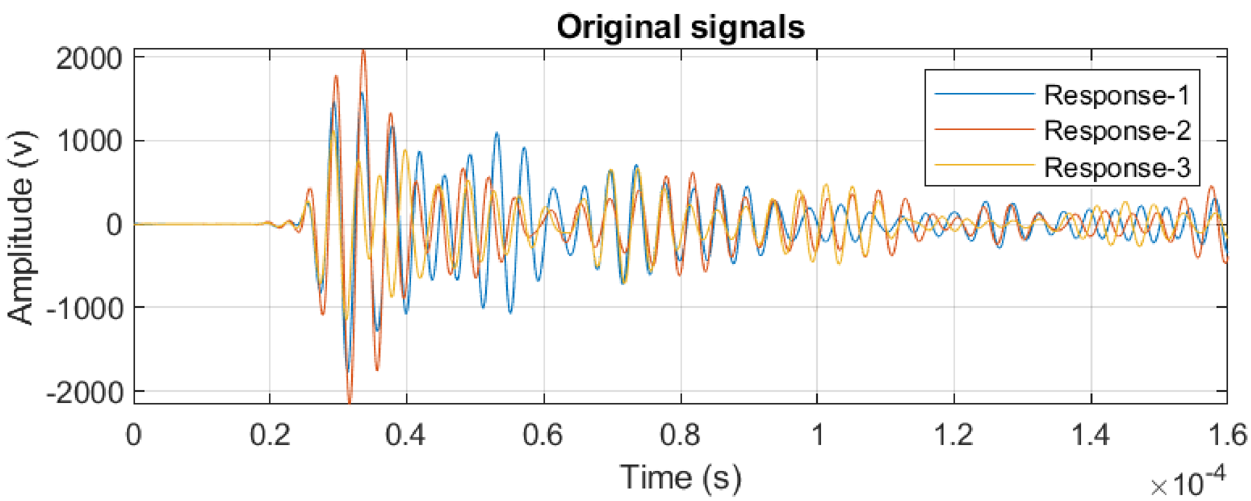

Figure 5.10 Received signals in time-domain.

To further solidify the effectiveness of these techniques in identifying fatigue damage in riveted panels and to conduct a comprehensive comparative analysis, we introduced a blind test case graciously provided by Boeing Corporation. It's essential to underscore that, before submitting the pertinent report to Boeing, we remained unaware of which specific signals corresponded to the actual damage. This added an extra layer of objectivity to our evaluation and underscores the reliability of our findings.

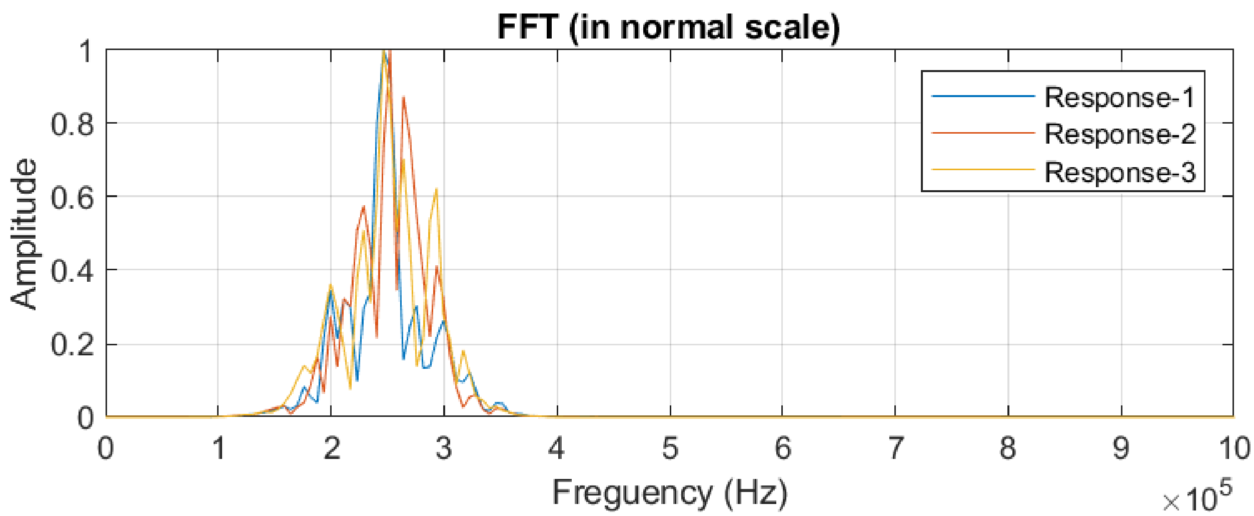

(a) Normal scale.

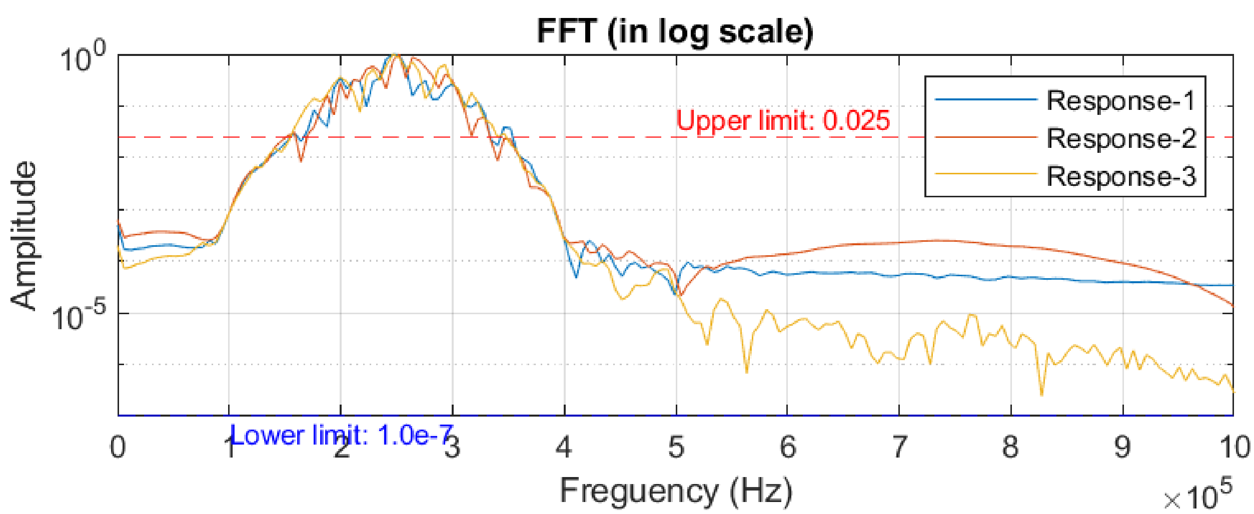

(b) Logarithmic scale.

Figure.5.11 FFTs of the two received signals: (a) Normal scale; and (b) Logarithmic scale.

The received signals in the time domain are depicted in Figure 5.10, each represented by a distinct color. The blind tests provided by Boeing include signals associated with fatigue cracking conditions as well as signals that do not indicate fatigue cracking, but all obtained from the same test coupon. The Fast Fourier Transform (FFT) results for these blind test signals are plotted in normal scale and log scale in Figures 5.11 (a) and (b), respectively. Based on the FFTs in log scale, the upper and lower limits can be established as 2.5×10^{-2} and 1×10^{-7}, respectively.

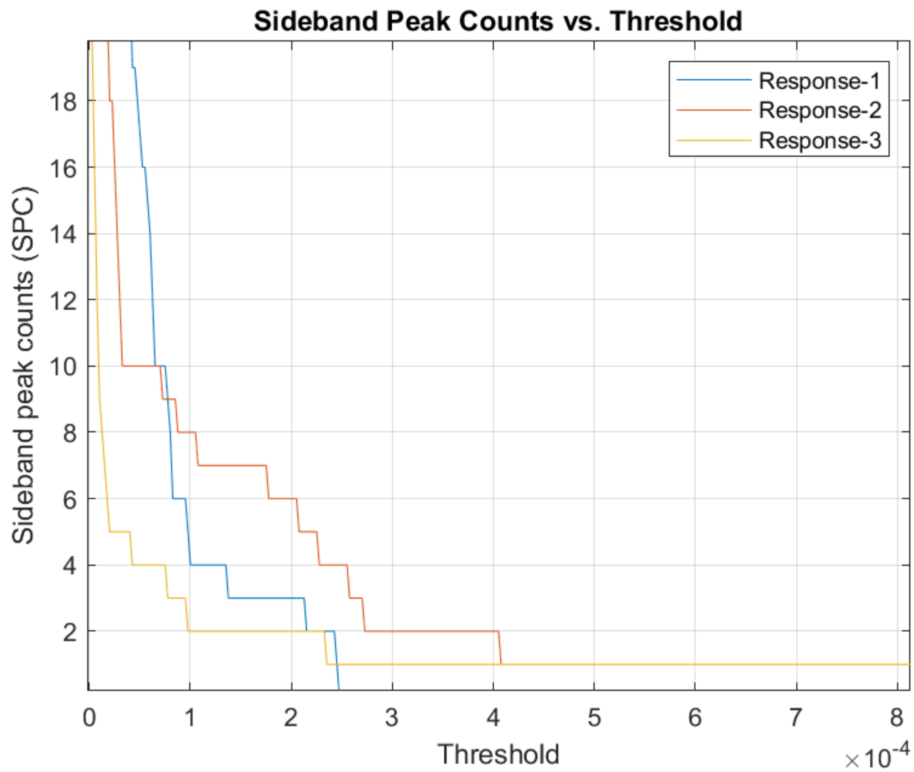

Figure 5.12 Sideband peak count (SPC) vs. threshold curve.

As shown in Figure 5.12, it is obviously that the SPC curves associated with fatigue crack is higher than the curve for undamaged cases. Figure 5.13 presents the SPC index values corresponding to various response signals. From these values, it is evident that some signals have a higher SPC index values, which indicates that this signal corresponds to the fatigue crack damage. In fact, according to Boeing Corporation's subsequent disclosure, it was confirmed that response 2 did indeed correspond to the path passing through the fatigue crack, and the actual crack length was approximately 0.2 inches.

It should be noted that such a crack length corresponds to the initial stage of a fatigue crack. SPC technology demonstrates sensitivity to even these small damages. Monitoring fatigue in its initial stages holds significant importance, not only for subsequent maintenance and inspection but also in averting the occurrence of catastrophic accidents. Detecting and addressing fatigue cracks early is critical in ensuring the safety and reliability of structures and equipment, reducing the risk of unexpected failures, and preventing potential disasters. Therefore, SPC technology is well-suited for monitoring the initial stages of fatigue cracks in rivet aluminum plates.

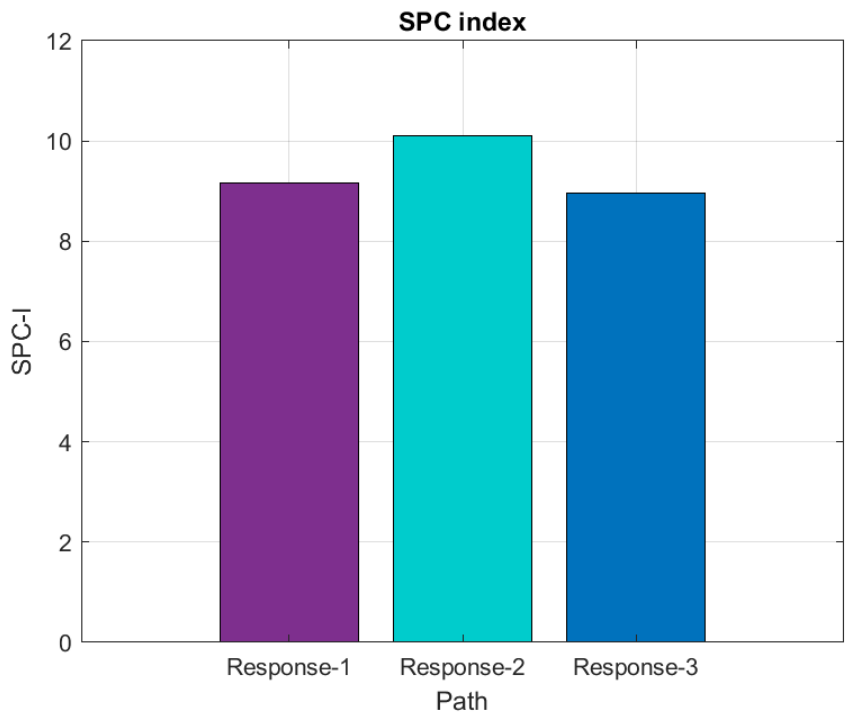

Figure 5.13 Sideband peak count (SPC) index

The cumulative sideband amplitude curves as shown in Figure 5.14 approximate horizontal lines when plotted against the threshold. This observation suggests that, as the threshold increases, there is minimal variation in the cumulative sideband amplitude for each individual signal. The curves remain nearly flat, indicating a consistent response within each signal. However, notable distinctions emerge when considering signals in comparison to each other. In the case of signals originating from fatigue cracks, their cumulative sideband amplitude values are significantly greater than those originating from undamaged signals. This phenomenon underscores that signals associated with fatigue cracks exhibit distinct and pronounced changes in their cumulative sideband amplitudes compared to undamaged signals when subjected to varying thresholds.

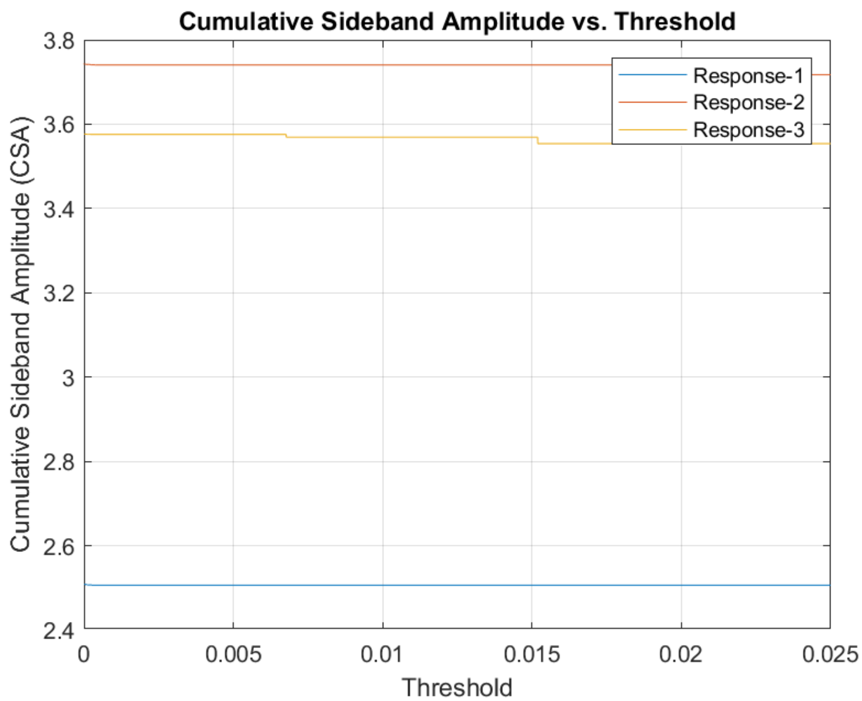

Figure 5.14 Cumulative sideband amplitude vs. threshold curve.

In Figure 5.15, corresponding SPI values for each response signal are presented. Notably, the response signal 2, which traverses the fatigue crack path, continues to exhibit a relatively higher SPI value. This observation aligns with the results obtained through the implementation of SPC technology. However, it is interesting to observe that the SPI value corresponding to response 1 is lower than the SPI value for response 3. This discrepancy suggests that response 3's signal, despite having no clearly visible fatigue crack around the rivet, exhibits a higher level of material nonlinearity compared to the rivet associated with response 1. These findings further emphasize the sensitivity of the SPI values in detecting material and structural changes, even in cases where visible fatigue cracks are absent.

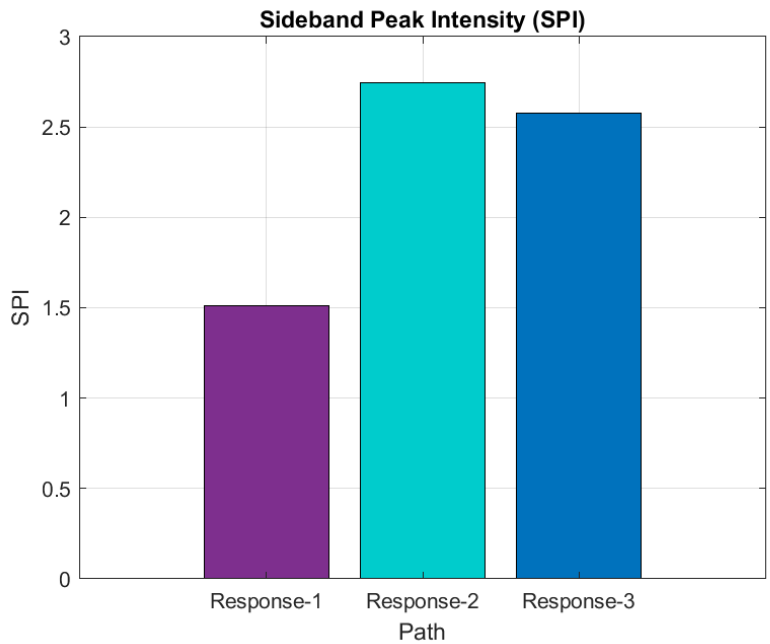

Figure 5.15 Cumulative sideband amplitude vs. threshold curve.

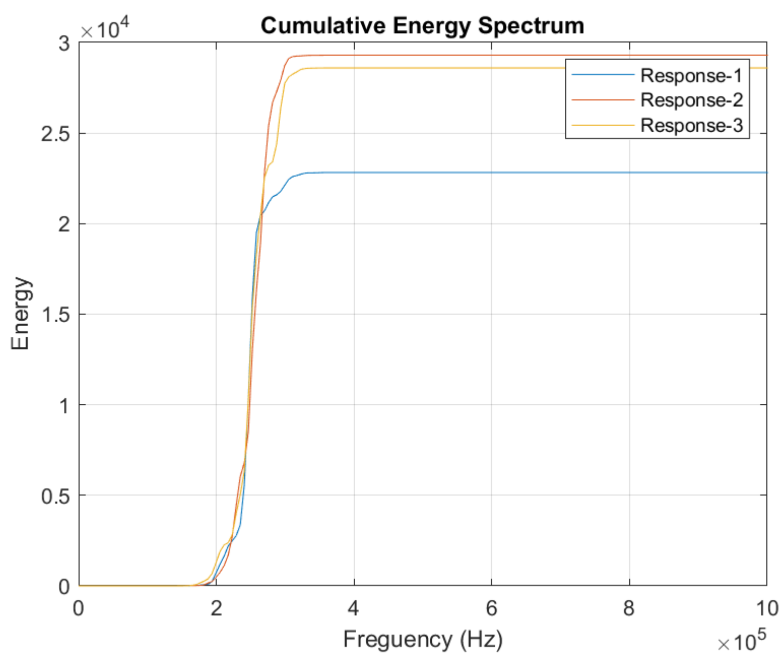

Figure 5.16 Cumulative spectral energy curve.

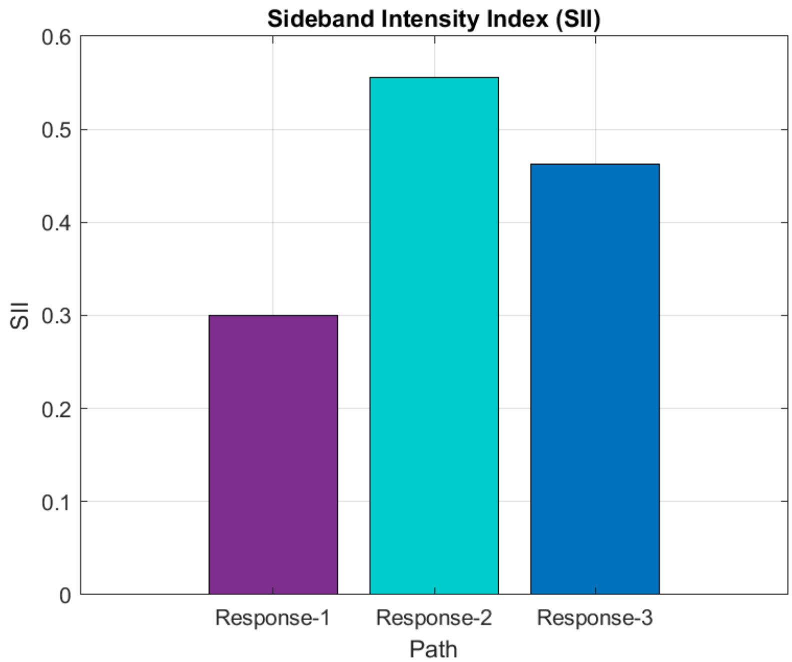

Figure. 5.17 Sideband intensity index (SII).

In Figure 5.16, the Cumulative Spectral Energy curves for the three blind test response signals are presented. Notably, the curves corresponding to response signals affected by fatigue cracks exhibit a more distinct curvature, particularly in the vicinity of the central frequency. This noticeable curvature can be attributed to the presence of Higher Harmonic Generation and SPG Sideband Peak Generation phenomena. These mechanisms result in an uneven distribution of energy within the signal's spectrum. In other words, as the response signals traverse fatigue crack paths, they undergo transformations that lead to the generation of higher harmonics and sideband peaks, causing the energy distribution to deviate from a more uniform pattern. This observation underscores the sensitivity of spectral analysis in identifying structural changes and the presence of fatigue cracks, even when they may not be visually evident.

In Figure 5.17, the signal strength index values for each response signal are depicted. Notably, these identification results closely align with the findings of the SPI technique, yet the SII index exhibits a higher level of differentiation. In essence, this means that the SII values corresponding to structural impairments are more prominently distinguished. Specifically, the SII value associated with response-1 is the lowest among the signals. This observation suggests that while no visible fatigue cracks were detected around the rivets corresponding to both response-1 and response-3, there is a slightly heightened degree of material nonlinearity around the rivet associated with response-2. This finding is consistent with the conclusions drawn from the SPI technique. It underscores the enhanced discriminatory capabilities of the SII index in identifying variations in material properties and structural conditions, which is particularly valuable when addressing situations where visible signs of fatigue cracking are absent.

Based on the provided information and the analysis of blind test results, it is evident that SPC, SPI, and SII techniques possess the capability to effectively identify fatigue cracks in their initial stages. The data presented in this analysis clearly demonstrates that these methods are proficient in distinguishing between signals associated with fatigue cracks and signals lacking visible damage. Such discrimination is of paramount importance for early detection and timely intervention, both of which are critical for ensuring the safety and reliability of structures and equipment.

It is worth noting that SPC, SPI, and SII exhibit varying levels of sensitivity, making them versatile tools for identifying structural impairments, even when there is no visual evidence of fatigue cracks. These findings collectively underscore the practicality of these techniques in monitoring the early stages of fatigue cracks in rivet aluminum plates. Moreover, they hold significant promise for enhancing the safety and maintenance of critical systems.

6. CONCLUSIONS

This research centers on employing newly developed nonlinear ultrasonic NDT&E techniques, such as the SPC, SPI, and SII techniques, to detect fatigue cracks in aircraft rivet aluminum plates. SII is the newest technique developed in this research. The mathematical proofs for higher harmonic generation (HHG) and sideband peak generation (SPG) in a more general scenario involving a set of frequencies are presented. Based on these analyses, the following conclusions can be drawn:

For fully linear materials, the response signal exhibits identical resonance frequencies as the exciting signal, i.e., ω_i (where $i = 1, \dots, N$). For moderately nonlinear materials, besides these frequencies ω_i (where $i = 1, \dots, N$), harmonic frequencies $2\omega_i$ (where $i = 1, \dots, N$), and modulated wave frequencies $\omega_i \pm \omega_k$ (where $1 \leq i < k \leq N$) are also generated. However, if the material exhibits much higher nonlinearity then in addition to the frequencies mentioned above, numerous additional higher harmonic frequencies and modulated wave frequencies arise, including $3\omega_i$ (where $i = 1, \dots, N$), $2\omega_i \pm \omega_k$ (where $1 \leq i < k \leq N$), as well as $\omega_i + \omega_k + \omega_l$, $\omega_i + \omega_k - \omega_l$, $\omega_i - \omega_k + \omega_l$, and $\omega_i - \omega_k - \omega_l$ (where $1 \leq i < k < l \leq N$).

A comprehensive review of various existing nonlinear ultrasonic techniques employed for assessing material nonlinearity is presented under the literature review. These techniques encompass Higher Harmonic Generation (HHG), the Frequency Modulation (FM) technique (also known as Nonlinear Wave Modulation Spectroscopy or NWMS), Nonlinear Impact Resonant Acoustic Spectroscopy (NIRAS) technique, and the Sideband Peak Count (SPC) technique. Furthermore, in response to the challenges associated with monitoring early fatigue cracks in riveted aluminum plates, a novel nonlinear acoustic technique known as the Sideband Intensity (SII) technique has been developed.

Finally, the applicability and effectiveness of SPC, SPI and newly developed SII techniques are evaluated using ultrasonic test data on riveted aluminum plates. The SPC technique possesses remarkable robustness and a multitude of advantages; however, its application requires adjustments to multiple parameters. The SPI technique can be regarded as a further refinement and a simplified version of SPC, overcoming the challenges associated with parameter adjustments. It provides a simplified noise handling technique without the need to fine-tune multiple variables for optimal performance. Nevertheless, the accurate detection of tiny fatigue cracks on riveted aluminum plates poses a significant challenge.

The proposed SII technique, which considers the spectral energy distribution of signals, with the foundation of SPC technology, offers an approach that doesn't necessitate frequent parameter adjustments. This combined approach proves effective in monitoring fatigue cracks on riveted aluminum plates and exhibits enhanced discriminative capabilities. However, it is important to point out that SII technology cannot entirely replace SPC-I technique. In reality, SPC technology offers greater flexibility, allowing for the individual monitoring of various types and sizes of damage.

REFERENCES

[1] National Transportation Safety Board. (2023). Aircraft Accident Investigation Report (Report No. AAB1302). https://www.ntsb.gov/investigations/AccidentReports/Reports/AAB1302.pdf

[2] National Transportation Safety Board. (2001). Aircraft Accident Report: Uncontrolled Descent and Collision with Terrain, US Air Flight 427, Boeing 737-300, N513AU Near Aliquippa, Pennsylvania, September 8, 1994 (Report No. NTSB/AAR-01/01). https://www.ntsb.gov/investigations/AccidentReports/Reports/AAR0101.pdf

[3] National Transportation Safety Board. (1999). Aircraft Accident Report: Crash During Landing, EgyptAir Flight 990, Boeing 767-366ER, SU-GAP Nantucket, Massachusetts, October 31, 1999 (Report No. NTSB/AAR-99/01). https://www.ntsb.gov/investigations/AccidentReports/Reports/AAR9901.pdf

[4] Chang Z. and Mal A. Scattering of Lamb waves from a rivet hole with edge cracks Mechanics of Materials Volume 31, Issue 3, March 1999, Pages 197-204

[5] Ihn JB and Chang FK. Detection and monitoring of hidden fatigue crack growth using a built-in piezoelectric sensor/actuator network: I. Diagnostics. Smart Mater Struct 2004; 13: 609–620.

[6] Ihn JB and Chang FK. Pitch-catch active sensing methods in structural health monitoring for aircraft structures. Struct Health Monit 2008; 7: 5–19.

[7] Ihn JB and Chang FK. Pitch-catch active sensing methods in structural health monitoring for aircraft structures. Struct Health Monit 2008; 7: 5–19.

[8] He, J., Guan, X., Peng, T., Liu, Y., Saxena, A., Celaya, J. R., and Goebel, K. A multi-feature integration method for fatigue crack detection and crack length estimation in riveted lap joints using Lamb waves. Smart Materials and Structures, 2013, 22(10), 105007.

[9] Biwa S, Nakajima S and Ohno N. On the acoustic nonlinearity of solid-solid contact with pressure-dependent interface stiffness. J Appl Mech 2004; 71(4): 508–515.

[10] Kim J-Y, Baltazar A, Hu JW, et al. Hysteretic linear and nonlinear acoustic responses from pressed interfaces. Int J Solids Struct 2006; 43(21): 6436–6452.

[11] Yan D, Drinkwater BW and Neild S. Measurement of the ultrasonic nonlinearity of kissing bonds in adhesive joints. NDT&E Int 2009; 42(5): 459–466.

[12] Hikata A and Elbaum C. Generation of ultrasonic second and third harmonics due to dislocations. Phys Rev 1966; 144(2): 469–477.

[13] Matlack KH, Kim J–Y, Jacobs LJ, et al. Review of second harmonic generation measurement techniques for material state determination in metals. J Nondestruct Eval 2015; 34(1): 273.

[14] Meegan GD, Johnson PA, Guyer RA, et al. Observations of nonlinear elastic wave behavior in sandstone. J Acoust Soc Am 1993; 94(6): 3387–3391.

[15] Shah AA, Ribakov Y and Hirose S. Nondestructive evaluation of damaged concrete using nonlinear ultrasonics.Mater Des 2009; 30(3): 775–782.

[16] Stauffer JD, Woodward CB and White KR. Nonlinear ultrasonic testing with resonant and pulse velocity parameters for early damage in concrete. ACI Mater J 2005; 102(2): 4–7.

[17] Cantrell JH and Yost WT. Nonlinear ultrasonic characterization of fatigue microstructures. Int J Fatigue 2001;23: S487–S490.

[18] Amura M, Meo M and Amerini F. Baseline-free estimation of residual fatigue life using a third order acoustic nonlinear parameter. J Acoust Soc Am 2011; 130(4): 1829–1837.

[19] Buck O, Morris WL and Richardson JM. Acoustic harmonic generation at unbonded interfaces and fatigue cracks. Appl Phys Lett 1978; 33(5): 371.

[20] Jhang K-Y and Kim K-C. Evaluation of material degradation using nonlinear acoustic effect. Ultrasonics 1999; 37(1): 39–44.

[21] Lv H, Jiao J, Wu B, et al. Evaluation of fatigue crack orientation using non-collinear shear wave mixing method. J Nondestruct Eval 2018; 37: 74.

[22] Li W, Xu Y, Hu N, et al. Impact damage detection in composites using a guided wave mixing technique. Meas Sci Technol 2019; 31: 1.

[23] Donskoy DM and Sutin AM. Vibro-acoustic modulation nondestructive evaluation technique. J Intell Mater Syst Struct 1998; 9: 765–771.

[24] Yoder NC and Adams DE. Vibro-acoustic modulation using a swept probing signal for robust crack detection. Struct Health Monit 2010; 9: 257–267.

[25] Sohn H, Lim HJ, DeSimio MP, et al. Nonlinear ultrasonic wave modulation for fatigue crack detection. J Sound Vib 2013; 333: 1473–1484.

[26] Chen XJ, Kim J–Y, Kurtis KE, et al. Characterization of progressive microcracking in Portland cement mortar using nonlinear ultrasonics. NDT&E Int 2008; 41: 112–118.

[27] Klepka A, Staszewski WJ, Jenal RB, et al. Nonlinear acoustics for fatigue crack detection—experimental investigations of vibro-acoustic wave modulations. Struct Health Monit 2012; 11: 197–211.

[28] Zhou C, Hong M, Su Z, et al. Evaluation of fatigue cracks using nonlinearities of acousto-

ultrasonic waves acquired by an active sensor network. Smart Mater Struct 2013; 22: 015018.

[29] Van Den Abeele KE-A, Carmeliet J, Ten Cate JA, et al. Nonlinear elastic wave spectroscopy (NEWS) techniques Alnuaimi et al. 149 to discern material damage. Part II: Single-mode nonlinear resonance acoustic spectroscopy. Res Nondestruct Eval 2000; 12(1): 31–42.

[30] Van Den Abeele KE-A, Johnson PA and Sutin A. Nonlinear elastic wave spectroscopy (NEWS) techniques to discern material damage. Part I: Nonlinear wave modulation spectroscopy (NWMS). Res Nondestruct Eval 2000; 12(1): 17–30.

[31] Eiras, J. N., Kundu, T., Bomilla, M., and Payá, J., 2013, "Nondestructive Monitoring of Ageing of Alkali Resistant Glass Fiber Reinforced Cement (GRC)," J Nondestruct Eval, 32(2–13), pp. 300–314.

[32] Liu, P., Sohn, H., Kundu, T., and Yang, S., 2014, "Noncontact Detection of Fatigue Cracks by Laser Nonlinear Wave Modulation Spectroscopy (LNWMS)," NDT&E Int., 66, pp. 106–116.

[33] Kundu, T., Eiras, J. N., Li, W., Liu, P., Sohn, H., and Paya, J., 2019, "Chapter 1," Fundamentals of Nonlinear Acoustical Techniques and Sideband Peak Count in Nonlinear Ultrasonic and Vibro-Acoustical Techniques for Nondestructive Evaluation, T. Kundu, ed., Springer Nature, Switzerland, pp. 1–88.

[34] Kundu, T., 2019, "Chapter 4," Nonlinear Ultrasonic Techniques for Nondestructive Evaluation in Mechanics of Elastic Waves and Ultrasonic Nondestructive Evaluation, T. Kundu, ed., CRC Press, Taylor and Francis Group, Boca Raton, FL.

[35] Alnuaimi, H., Amjad, U., Russo, P., Lopresto, V., and Kundu, T., 2021, "Monitoring Damage in Composite Plates From Crack Initiation to Macro-Crack Propagation Combining Linear and Nonlinear Ultrasonic Techniques," Struct. Health Monitor., 20(1), pp. 139–150.

[36] Basu, S., Thirumalaiselvi, A., Sasmal, S., and Kundu, T., 2021, "Nonlinear Ultrasonics Based Technique for Monitoring Damage Progression in Reinforced Concrete Structures," Ultrasonics, 115,p. 106472.

[37] Arumaikani, T., Sasmal, S., and Kundu, T., 2021, "Detection of Initiation of Corrosion Induced Damage in Concrete Structures Using Nonlinear Ultrasonic Techniques," J. Acoust. Soc. Am., 151(2), p.1341-1352.

[38] Castellano, A., Fraddosio, A., Piccioni, M. D., and Kundu, T., 2021, "Linear and Nonlinear Ultrasonic Techniques for Monitoring Stress-Induced Damages in Concrete," ASME J. Nondestruct. Eval., 4(4), p. 041001.

[39] Nikvar-Hassani, A., Alnuaimi, H. N., Amjad, U., Sasmal, S., Zhang, L., and Kundu, T., 2022, “Alkali Activated Fly Ash Based Concrete: Evaluation of Curing Process Using Non-Linear Ultrasonic Approach,” ASME J. Nondestruct. Eval., 5(2), p. 021006.

[40] Alnuaimi, H., Amjad, U., Park, S., Russo, P., Lopresto, V., and Kundu, T., 2022, “An Improved Nonlinear Ultrasonic Technique for Detecting and Monitoring Impact Induced Damage in Composite Plates,” Ultrasonics, 119, p 106620.

[41] Van Den Abeele, K.E.-A., Sutin, A.M., Carmeliet, J. & Johnson, P.A. Micro-damage diagnostics using nonlinear elastic wave spectroscopy (NEWS). NDT & E International 34, 239-248 (2001).

[42] Eiras, J. N., Kundu, T., Bomilla, M., and Payá, J., 2013, “Nondestructive Monitoring of Ageing of Alkali Resistant Glass Fiber Reinforced Cement (GRC),” J Nondestruct Eval, 32(2–13), pp. 300–314.

[43] Liu, P., Sohn, H., Kundu, T., and Yang, S., 2014, “Noncontact Detection of Fatigue Cracks by Laser Nonlinear Wave Modulation Spectroscopy (LNWMS),” NDT&E Int., 66, pp. 106–116.

[44] Alnuaimi, H., Amjad, U., Russo, P., Lopresto, V., and Kundu, T., 2021, “Monitoring Damage in Composite Plates From Crack Initiation to Macro-Crack Propagation Combining Linear and Nonlinear Ultrasonic Techniques,” Struct. Health Monitor., 20(1), pp. 139–150.

[45] Alnuaimi, H., Amjad, U., Park, S., Russo, P., Lopresto, V., and Kundu, T., 2022, “An Improved Nonlinear Ultrasonic Technique for Detecting and Monitoring Impact Induced Damage in Composite Plates,” Ultrason., 119, p. 106620.

[46] Castellano, A., Fraddosio, A., Piccioni, M. D., and Kundu, T., 2021, “Linear and Nonlinear Ultrasonic Techniques for Monitoring Stress-Induced Damages in Concrete,” ASME J. Nondestruct. Eval., 4(4), p. 041001.

[47] Nikvar-Hassani, A., Alnuaimi, H. N., Amjad, U., Sasmal, S., Zhang, L., and Kundu, T., 2022, “Alkali Activated Fly Ash Based Concrete: Evaluation of Curing Process Using Non-Linear Ultrasonic Approach,” ASME J. Nondestruct. Eval., 5(2), p. 021006.

[48] Park, S., and Kundu, T., 2023, “A modified sideband peak count based nonlinear ultrasonic technique for material characterization,” Ultrasonics, 128, p. 106585

[49] Kelkar, S. S., Grigsby, L. L., & Langsner, J. An extension of Parseval’s theorem and its use in calculating transient energy in the frequency domain. IEEE Transactions on Industrial Electronics,1983, IE-30(1), 42–45.